Journal of Visualized Experiments
Measuring 3D in-vivo shoulder kinematics using biplanar videoradiography
--Manuscript Draft--

Article Type:	Invited Methods Collection - JoVE Produced Video
Manuscript Number:	JoVE62210R2
Full Title:	Measuring 3D in-vivo shoulder kinematics using biplanar videoradiography
Corresponding Author:	Michael Bey Henry Ford Health System Detroit, MI UNITED STATES
Corresponding Author's Institution:	Henry Ford Health System
Corresponding Author E-Mail:	bey@bjc.hfh.edu
Order of Authors:	Rebekah Lawrence
	Roger Zauel
	Michael Bey
Additional Information:	
Question	**Response**
Please specify the section of the submitted manuscript.	Bioengineering
Please indicate whether this article will be Standard Access or Open Access.	Standard Access (US$2,400)
Please indicate the **city, state/province, and country** where this article will be **filmed**. Please do not use abbreviations.	Detroit, MI USA
Please confirm that you have read and agree to the terms and conditions of the author license agreement that applies below:	I agree to the Author License Agreement
Please provide any comments to the journal here.	

1   **TITLE:**
2   Measuring 3D In-vivo Shoulder Kinematics using Biplanar Videoradiography
3
4   **AUTHORS AND AFFILIATIONS:**
5   Rebekah L. Lawrence, Roger Zauel, Michael J. Bey
6
7   Bone and Joint Center, Department of Orthopaedic Surgery, Henry Ford Health System, Detroit,
8   MI, US
9
10   Email addresses of co-authors:
11   Rebekah L. Lawrence   (rlawren2@hfhs.org)
12   Roger Zauel   (rzauel1@hfhs.org)
13   Michael J. Bey   (bey@bjc.hfh.edu)
14
15   Corresponding author
16   Michael J. Bey   (bey@bjc.hfh.edu)
17
22   **SUMMARY:**
23   Biplane videoradiography can quantify shoulder kinematics with a high degree of accuracy. The
24   protocol described herein was specifically designed to track the scapula, humerus, and the ribs
25   during planar humeral elevation, and outlines the procedures for data collection, processing, and
26   analysis. Unique considerations for data collection are also described.
27

28   **ABSTRACT:**
29   The shoulder is one of the human body's most complex joint systems, with motion occurring
30   through the coordinated actions of four individual joints, multiple ligaments, and approximately
31   20 muscles. Unfortunately, shoulder pathologies (e.g., rotator cuff tears, joint dislocations,
32   arthritis) are common, resulting in substantial pain, disability, and decreased quality of life. The
33   specific etiology for many of these pathologic conditions is not fully understood, but it is generally
34   accepted that shoulder pathology is often associated with altered joint motion. Unfortunately,
35   measuring shoulder motion with the necessary level of accuracy to investigate motion-based
36   hypotheses is not trivial. However, radiographic-based motion measurement techniques have
37   provided the advancement necessary to investigate motion-based hypotheses and provide a
38   mechanistic understanding of shoulder function. Thus, the purpose of this article is to describe
39   the approaches for measuring shoulder motion using a custom biplanar videoradiography
40   system. The specific objectives of this article are to describe the protocols to acquire biplanar
41   videoradiographic images of the shoulder complex, acquire CT scans, develop 3D bone models,
42   locate anatomical landmarks, track the position and orientation of the humerus, scapula, and
43   torso from the biplanar radiographic images, and calculate the kinematic outcome measures. In
44   addition, the article will describe special considerations unique to the shoulder when measuring

45   joint kinematics using this approach.

46

47   **INTRODUCTION:**

48   The shoulder is one of the human body's most complex joint systems, with motion occurring

49   through the coordinated actions of four individual joints, multiple ligaments, and approximately

50   20 muscles. The shoulder also has the greatest range of motion of the body's major joints and is

51   often described as a compromise between mobility and stability. Unfortunately, shoulder

52   pathologies are common, resulting in substantial pain, disability, and decreased quality of life.

53   For example, rotator cuff tears affect about 40% of the population over age 60[1–3], with

54   approximately 250,000 rotator cuff repairs performed annually[4], and an estimated economic

55   burden of $3–5 billion per year in the United States[5]. Additionally, shoulder dislocations are

56   common and are often associated with chronic dysfunction[6]. Lastly, glenohumeral joint

57   osteoarthritis (OA) is another significant clinical problem involving the shoulder, with population

58   studies indicating that roughly 15%–20% of adults over the age of 65 have radiographic evidence

59   of glenohumeral OA[7,8]. These conditions are painful, impair activity levels, and decrease quality

60   of life.

61

62   Although the pathogeneses of these conditions are not fully understood, it is generally accepted

63   that altered shoulder motion is associated with many shoulder pathologies[9–11]. Specifically,

64   abnormal joint motion may contribute to the pathology[9,12], or that the pathology may lead to

65   abnormal joint motion[13,14]. Relationships between joint motion and pathology are likely complex,

66   and subtle alterations in joint motion may be important in the shoulder. For example, although

67   angular motion is the predominant motion occurring at the glenohumeral joint, joint translations

68   also occur during shoulder motion. Under normal conditions these translations likely do not

69   exceed several millimeters[15–19], and therefore may be below the level of in-vivo accuracy for

70   some measurement techniques. While it may be tempting to assume that small deviations in

71   joint motion may have little clinical impact, it is important to also recognize that the cumulative

72   effect of subtle deviations over years of shoulder activity may exceed the individual's threshold

73   for tissue healing and repair. Furthermore, in-vivo forces at the glenohumeral joint are not

74   inconsequential. Using custom instrumented glenohumeral joint implants, previous studies have

75   shown that raising a 2 kg weight to head height with an outstretched arm can result in

76   glenohumeral joint forces that can range from 70% to 238% of body weight[20–22]. Consequently,

77   the combination of subtle changes in joint motion and high forces concentrated over the

78   glenoid's small load-bearing surface area may contribute to the development of degenerative

79   shoulder pathologies.

80

81   Historically, the measurement of shoulder motion has been accomplished through a variety of

82   experimental approaches. These approaches have included the use of complex cadaveric testing

83   systems designed to simulate shoulder motion[23–27], video-based motion capture systems with

84   surface markers[28–31], surface-mounted electromagnetic sensors[32–35], bone pins with reflective

85   markers or other sensors attached[36–38], static two-dimensional medical imaging (i.e.,

86   fluoroscopy[39–41] and radiographs[17,42–45]), static three-dimensional (3D) medical imaging using

87   MRI[46,47], computed tomography[48], and dynamic, 3D single plane fluoroscopic imaging[49–51]. More

88   recently, wearable sensors (e.g., inertial measurement units) have gained popularity for

89   measuring shoulder motion outside the laboratory setting and in free-living conditions[52–57].

90

91   In recent years, there has been a proliferation of biplane radiographic or fluoroscopic systems
92   designed to accurately measure dynamic, 3D in-vivo motions of the shoulder[58–62]. The purpose
93   of this article is to describe the authors' approach for measuring shoulder motion using a custom
94   biplanar videoradiography system. The specific objectives of this article are to describe the
95   protocols to acquire biplanar videoradiographic images of the shoulder complex, acquire CT
96   scans, develop 3D bone models, locate anatomical landmarks, track the position and orientation
97   of the humerus, scapula, and torso from the biplanar radiographic images, and calculate
98   kinematic outcome measures.

99

100   **PROTOCOL:**
101   Prior to data collection, the participant provided written informed consent. The investigation was
102   approved by Henry Ford Health System's Institutional Review Board.

103

104   Protocols for acquiring, processing, and analyzing biplane radiographic motion data are highly
105   dependent up on the imaging systems, data processing software, and outcome measures of
106   interest. The following protocol was specifically designed to track the scapula, humerus, and the
107   third and the fourth ribs during scapular-plane or coronal-plane abduction and quantify
108   glenohumeral, scapulothoracic, and humerothoracic kinematics.

109

110   **1. CT imaging protocol**

111

112   1.1   Ask the participant to lie onto the CT examination table with their arms at their sides.
113   Depending on the participant's size, position them off center on the table such that the entire
114   hemi-torso is available for imaging.

115

116   1.2   To acquire the scout images, the technologist ensures to include the clavicle
117   (superiorly), the distal humeral epicondyles (inferiorly), the entire glenohumeral joint (laterally),
118   and the costovertebral and sternocostal joints (medially) in the CT field of view includes (**Figure**
119   **1**).

120

121   1.3   Acquire the CT scan with the following parameters: scan mode = helical; tube voltage =
122   120 kVp; tube current: 200–400 mA (auto); slice thickness = 0.66 mm; FOV = 34 cm.

123

124   1.4   Verify the scan quality and the field of view.

125

126   1.5   Reformat the acquisition using an image matrix size of 512 x 512 pixels. Given the slice
127   thickness and FOV, the acquisition results in an isotropic voxel spacing of 0.66 mm.

128

129   1.6   Export the images in DICOM format.

130

131   **2. Biplane X-ray motion capture protocol**

132

NOTE: The custom biplanar x-ray system used in this protocol is described in the **Table of Materials**. Data collection procedures will likely vary with different system components. The x-ray systems are arbitrarily termed "green" and "red" to distinguish procedures and resulting image sequences and are positioned with an approximately 50° inter-beam angle and a source-to-image distance (SID) of approximately 183 cm (

Figure *1*: The CT field of view. (**A**) coronal, (**B**) sagittal, and (**C**) transverse planes. During acquisition, the CT technologist ensures the field of view includes the clavicle (superiorly), the distal humeral epicondyles (inferiorly), the entire glenohumeral joint (laterally), and the costovertebral and sternocostal joints (medially).

**Figure *2*). A minimum of two research personnel are required for the data collection; one to operate the x-ray system and computer, and the other to instruct the research participant.

2.1   Camera software setup

2.1.1   Set the camera aperture to the default setting (f/5.6).

NOTE: This value depends on several factors, including camera, exposure time, ISO, and participant anthropometrics.

2.1.2   Open the camera software and load the study protocol to each camera (sampling rate: 60 Hz, exposure time: 1,100 μs).

NOTE: The camera exposure time may vary depending on several factors, including camera, aperture setting, and radiographic exposure.

2.2   System warmup

NOTE: The x-ray tube's anode may become damaged if high-powered exposures are produced when it is cold. Therefore, the tubes should be warmed up by a series of low-energy exposures based on the manufacturer's recommendations.

2.2.1   On both the x-ray generator control panels, select **Vascular** setting. The pre-programmed vascular settings produce low energy exposures appropriate for the system warm-up (per system manufacturer).

2.2.2   Set the exposure time on the pulse generator to 0.25 s.

2.2.3   On the x-ray generator control panels, hold down the **PREP** buttons. **Preparation Delay** appears on the screen.

2.2.4   Once both the screens read **Ready to Expose**, simultaneously press and hold the **EXPOSE** buttons.

177 NOTE: This will not produce x-rays, but only arms the system. X-ray production only occurs by
178 depressing the foot pedal or hand-held triggers.

179

180 2.2.5   Depress the **PREP** and **EXPOSE** buttons on both the control panels, and simultaneously
181 depress and hold the foot pedal (or hand-held) to trigger the x-ray generator to produce x-rays.

182

183 NOTE: The x-rays are produced for the duration specified by the pulse generator (step 2.3.2) or
184 until the pedal is released, whichever occurs first.

185

186 2.2.6   Repeat the steps 2.2.2–2.2.5 until the x-ray tube's heat unit (HU) exceeds the level
187 required by the manufacturer to acquire images (5% HU for our system).

188

189 2.3   Verify the camera synchronization and image focus.

190

191 NOTE: Verify the camera synchronization and focus by acquiring a set of test images of the
192 distortion correction grid (see **Table of Materials**). Each image intensifier will be tested
193 individually using the steps described below.

194

195 2.3.1   Place the distortion correction grid on the image intensifier.

196

197 2.3.2   On both x-ray generator control panels, select the **Cardiac** setting, which is programmed
198 to the default radiographic technique (70 kVp, 320 mA, 2 ms, and focal spot = 1.0 mm).

199

200 NOTE: The camera settings remain unchanged (sampling rate: 60 Hz, exposure time: 1,100 µs).

201

202 2.3.3   Set the pulse generator to 0.25 s.

203

204 2.3.4   Initiate the camera acquisition through the camera software and acquire x-ray images as
205 described previously in the steps 2.2.3–2.2.5.

206

207 2.3.5   Preview the resulting images and determine the elapsed time from the trigger pulse for
208 each system. If the difference in elapsed time between cameras is more than 2 µs, determine the
209 camera which is firing late and specify a frame delay in the camera software to resolve the issue.

210

211 2.3.6   Visually inspect the sharpness of the image to verify the camera focus. For objective
212 assessment, analyze a profile line drawn across a bead within the distortion correction grid using
213 an image processing software (e.g., ImageJ). Specifically, inspect the slope of the pixel gray values
214 along this profile line. A more negative slope ensures a sharper image (assuming radiographic
215 image is inverted such that the bead is dark). If necessary, refocus the cameras and repeat the
216 steps 2.3.3–2.3.6.

217

218 2.4   Research participant setup and positioning

219

NOTE: The research participant's positioning is highly dependent upon the bones being tracked and the motion being tested. Testing is typically performed with the research participant seated on a fixed chair (i.e., not swivel or wheeled) to minimize the potential for changes in their position that may cause the shoulder to move outside the 3D imaging volume.

2.4.1   Position the chair in the biplane imaging volume so that the shoulder to be tested is centered approximately where the biplane x-ray beams intersect. This is a preliminary position. Adjust it based on the participant's anthropometrics, the motion to be tested, and the bones to be tracked.

2.4.2   Ask the participant to be seated in a comfortable upright posture with arms resting at his/her side.

2.4.3   Secure a lead-lined protective vest across the participant's torso to cover their abdomen and the contralateral shoulder and chest.

2.4.4   Set the preliminary height of the image intensifiers. To help inform this procedure, turn on the light within the system's x-ray source. Raise the system until the participant's shadow cast onto the image intensifier is at the level of their axilla.

NOTE: The source and image intensifier within each system are coupled to move together. Uncoupled systems will require additional alignment steps not described here.

2.4.5   Establish the preliminary height of the image intensifiers. Gently move the participant on their chair within the biplane image volume while watching their shadow cast onto the image intensifier.

NOTE: A good initial guess is to have the participant positioned such that the acromioclavicular joint is approximately at the center of both image intensifiers. This position is a reasonable initial guess for the current protocol, which requires the visualization and tracking of the humerus, scapula, and two ribs during shoulder elevation.

2.4.6   Once the participant's position appears to be reasonable in both systems, keep the light source on and ask the participant to perform the motion to be tested. Ensure that the participant's shoulder remains within the radiographic field of view during the entire motion trial. If possible, collimate x-ray beams to reduce exposure.

2.4.7   Repeat the steps 2.4.5–2.4.6 until it appears that the participant's setup within the image volume is appropriate.

2.4.8   Researcher #1: Return to the control room to run the x-ray control panels and cameras. Set the x-ray control panel to low power fluoroscopy mode (60 kVp, 3–4 mA) and the pulse generator to a 0.25 s acquisition.

264 **2.4.9** Researcher #2: Explain to the participant that an image will be taken so that their position
265 can be verified in the images and describe the series of events that will happen. Warn the
266 participant about the sounds the system makes (e.g., clicks, hums) to prevent any apprehension.
267 Don a lead-lined protective vest, retrieve the hand-held trigger, move as far away from the x-ray
268 sources as possible to minimize exposure while still maintaining a clear line of sight and
269 communication with the participant. If possible, stand behind a lead-lined shield with a window.
270
271 **2.4.10** Researcher #1 (in x-ray control room): Start the cameras and prime the x-ray control panel
272 as described previously (steps 2.2.3–2.2.5). When the system is ready to expose, notify the
273 researcher #2.
274
275 **2.4.11** Researcher #2 (in lab): Indicate to the participant about image acquisition. Trigger the
276 radiographic image acquisition using the hand-held remote trigger. Inform the participant that
277 an image was taken and excuse yourself to the control room.
278
279 **2.4.12** Researcher #1 and #2 (in x-ray control room): Inspect the images. Focus only on the
280 participant's position and the visibility of all bones to be tracked. If necessary, repeat steps 2.4.5–
281 2.4.12 until the participant's position is satisfactory.
282
283 **2.4.13** Once the setup and positioning of the x-ray system is established, do not move the x-ray
284 system during the data collection session unless new calibration and distortion correction images
285 are collected for each configuration. Also, instruct the participant to move as little as possible for
286 the duration of the data collection session to avoid having to repeat setup procedures.
287
288 **2.5** Data collection: Static image acquisition
289
290 **2.5.1** Researcher #1 (in x-ray control room): Set the optimized radiographic technique on the x-
291 ray control panel (based on preliminary testing). The radiographic protocol used here is 70 kVp,
292 320 mA, 2 ms, and focal spot = 1.0 mm, with the camera collecting at 60 Hz and an exposure time
293 of 1,100 μs. Set the pulse generator to 0.25 s.
294
295 NOTE: Inform the participant that the next image will be a formal image acquisition.
296
297 **2.5.2** Researcher #2 (in the lab): Inform the participant to sit upright with their arm resting at
298 their side.
299
300 **2.5.3** Acquire an image as previously described (steps 2.4.8–2.4.11).
301
302 **2.5.4** Researchers #1 and #2 (in x-ray control room): Inspect the images. Focus on the image
303 quality (i.e., brightness and contrast) and visibility of all necessary bones. If adjustments to the
304 image quality are needed, determine the parameter to be modified (i.e., f-stop, camera exposure
305 time, kVp, mA) and reacquire the static image.
306

307 NOTE: It is critical to always be mindful of how the dose is affected by the radiographic
308 parameters.

310 2.5.5   Repeat steps 2.5.1–2.5.4 until the image quality is acceptable, within the dose estimates
311 approved by the IRB.

313 2.5.6   Once the image quality is acceptable, inspect the images for technical quality (e.g.,
314 corrupt frames).

316 2.5.7   After an acceptable static trial image acquisition, save the trial from each camera (e.g.,
317 "green_still.cine", "red_still.cine").

319 2.6   Data Collection: Dynamic image acquisition

321 2.6.1   Researcher #1 (in x-ray control room): Maintain the same radiographic parameters from
322 the static trial image. Set the pulse generator to a 2.0 s exposure.

324 2.6.2   Researcher #2 (in the lab): Teach the participant the motion to be performed, including
325 the plane and timing of the motion. Verify that the chair and the participant's clothing and/or
326 lead-lined vest do not interfere with the shoulder motion. Practice the motion trial with the
327 participant. Use the verbal cue "Ready…and…go" paced so that it takes 2 s (i.e., the duration of
328 the motion trial) to help the participant pace the initiation and completion of the motion.

330 NOTE: It is critical that the participant understands the procedures and can consistently perform
331 the motion trial to avoid the unnecessary exposure associated with a failed trial.

333 2.6.3   Researcher #2 (in the lab): After sufficient practice, retrieve the hand-held remote trigger.
334 Move to a safe place in the lab with a clear line of sight and communication with the research
335 participant.

337 2.6.4   Researcher #1 (in x-ray control room): Reset the pulse generator to 2.0 s, start the
338 cameras, and prime the x-ray control panel as described previously (steps 2.3.4–2.3.5). When the
339 system is ready to expose, notify the researcher #2.

341 2.6.5   Researcher #2 (in lab): Ask the research participant, "Are you ready?" [wait for the
342 affirmative response] "Ready…and…go." (paced, as before, so that it takes 2 s).

344 2.6.6   Researcher #2 (in lab): Manually trigger the x-ray system when the participant initiates
345 arm motion.

347 NOTE: Although manually triggering based on visual motion risks omitting the onset of the
348 motion trial, it prevents over-exposing the research participant in the event of a
349 miscommunication or a delayed start.). Once the trial is complete, inform the participant that an
350 image was taken and excuse yourself to the control room to inspect the images.

351

<mark>2.6.7   Researchers #1 and #2 (in x-ray control room): Inspect the trial images for quality (i.e., brightness and contrast) and technical condition (i.e., any corrupt frames) (**Figure 3**). Save the motion trials from each camera (e.g., "green_scapab1.cine", "red_scapab1.cine").</mark>

<mark>2.6.8   Repeat the steps 2.6.1–2.6.7 to collect all the motion trials within the approved radiation safety protocol.</mark>

2.7   Collect calibration images

NOTE: Radiographic image calibration results in the definition of the laboratory-based coordinate system, the position and orientation of each x-ray radiographic system relative to laboratory coordinate system, and intrinsic parameters that allow for the generation of digitally reconstructed radiographs (DRRs), which are used in the markerless tracking process. The calibration calculations are described in the step 3.4.1.

2.7.1   Maintain the same camera settings and radiographic technique settings used during the data collection.

2.7.2   Set the pulse generator to a 0.5 s exposure.

2.7.3   Position the calibration cube (see **Table of Materials**) in the middle of the imaging volume.

2.7.4   Acquire and save the cube images (e.g., "green_cube.cine", "red_cube.cine").

2.8   Collect the images for distortion correction and nonuniformity correction.

NOTE: Radiographic image collected using an image intensifier are affected by intensity, nonuniformity[63], and distortion. Consequently, images of a white-field and distortion correction grid are acquired on each radiographic system to determine the corrections needed. It is generally prudent to collect calibration images before distortion and nonuniformity correction images in case the image intensifiers are bumped while the distortion grid is being positioned.

2.8.1   Remove all objects from the radiographic field of view.

2.8.2   Maintain the same camera settings and radiographic technique settings used during the data collection. Set the pulse generator to a 0.5 s exposure.

2.8.3   Attach the distortion correction grid (see **Table of Materials**) to the surface of the green image intensifier.

2.8.4   Acquire the grid and white-field images.

2.8.5   Save the images (e.g., "green_grid.cine", "red_white.cine").

395

396   2.8.6   Move the grid to the red image intensifier and repeat the steps 2.7.2–2.7.5.

397

398   **3   Data processing protocol**

399

400   NOTE: Procedures for preparing the bony geometry, image pre-processing (i.e., distortion and
401   non-uniformity correction and image calibration), and markerless tracking are highly variable and
402   depend on the software used. The procedures described herein are specific to the proprietary
403   software. However, the major data processing steps are likely translatable to any x-ray motion
404   capture software package.

405

406   3.1   Processing CT scan

407

408   NOTE: The proprietary markerless tracking software used by the authors' lab optimizes the
409   position and orientation of a DRR. Therefore, the procedures for processing the CT scan results
410   in the creation of a 16-bit TIFF image stack. Other software packages may require the bony
411   geometry to be represented in different formats or specifications.

412

413   3.1.1   Open an image processing program (e.g., Mimics, FIJI) and import the CT images.

414

415   3.1.2   Segment the humerus from the surrounding soft tissues. For the ribs, create an extension
416   that connects the anterior aspect of the rib to the manubrium to digitize the sternocostal joint
417   later in step 3.2.6.

418

419   3.1.3   Perform a Boolean operation on the finished mask with a black mask (i.e., all pixels are
420   colored black) (operation: black minus bone). This results in an inverted mask of the bone in
421   which all pixels are black except for those corresponding to the bone, which remain in CT
422   grayscale.

423

424   3.1.4   Crop the image stack along all three axes to eliminate the black (i.e., non-bone) pixels.
425   Leave some black pixels at the edges of this 3D bounding box.

426

427   3.1.5   Save the modified image stack in the TIFF format.

428

429   3.1.6   Repeat the steps 3.1.1–3.1.5 for all the remaining bones.

430

431   3.2   Defining anatomical coordinate systems and regions of interest (ROIs)

432

433   NOTE: This protocol orients anatomical coordinate systems as follows. For a right shoulder, the
434   +X axis is oriented laterally, the +Y axis is oriented superiorly, and the +Z axis is oriented
435   posteriorly. For a left shoulder, the +X axis is oriented laterally, the +Y axis is oriented superiorly,
436   and the +Z axis is oriented anteriorly.

437

438   3.2.1   Import the TIFF image stack for the bone to be processed. Convert the TIFF stack to a
439   .RAW file and render a 3D bone model based on the known pixel dimensions and image spacing
440   using the proprietary software.
441
442   NOTE: The resolution of the model is based on the sampling of the CT volume (i.e., voxel spacing).
443   Consequently, the average area of the mesh triangles is approximately 1.02 mm^2 (±0.2 mm^2)
444   (step 1.3).
445
446   3.2.2   Digitize the anatomical landmarks on the humerus as follows (**Figure 4A**).
447
448   3.2.2.1 Geometric center of the humeral head: Determine the dimensions and position of a
449   sphere that minimizes the distance between the sphere's surface and the humeral articular
450   surface using a least-squares algorithm. Determine the geometric center of the humeral head as
451   the coordinates of the optimized sphere's center.
452
453   3.2.2.2 Medial and lateral epicondyles: Located at the widest section of the distal humerus.
454
455   3.2.3   Define humeral head ROI as follows (**Figure 5A**).
456
457   3.2.3.1 The entire humeral articular surface and greater tuberosity.
458
459   3.2.4   Digitize the anatomical landmarks on the scapula as follows (**Figure 4B**).
460
461   3.2.4.1 Root of the scapular spine: Located at the medial border along the scapular spine.
462
463   3.2.4.2 Posterior acromioclavicular joint: Located at the posterior aspect of the clavicular facet
464   on the scapular acromion.
465
466   3.2.4.3 Inferior angle: Located at the inferior-most point on the scapula.
467
468   3.2.5   Define scapular ROIs as follows (**Figure 5B**).
469
470   3.2.5.1 Acromion: The undersurface of the acromion lateral to the spine of the scapula.
471
472   3.2.5.2 Glenoid: The entire articulating surface of the glenoid.
473
474   3.2.6   Digitize anatomical landmarks on the ribs as follows (**Figure 4C**).
475
476   3.2.6.1 Anterior rib: Located at the medial-most portion of the rib extension.
477
478   3.2.6.2 Posterior rib: Located at the superior/inferior midpoint of the posterior aspect of the facet
479   on the head of the rib.
480

481 3.2.6.3 Lateral rib: Located at the lateral-most aspect of the rib when the anterior and posterior
482 rib points are aligned vertically on the screen.
483
484 3.3   Image pre-processing
485
486 NOTE: Image pre-processing is performed using proprietary software and involves converting the
487 cine image files to TIFF stacks and correcting the images for distortion nonuniformity.
488
489 3.3.1   Perform non-uniformity correction: The software averages the approximately 30 frames
490 (i.e., 0.5 s of data) to produce a single, high-quality, bright-field image to minimize the effect of
491 noise in any single frame. The bright-field image is used to calculate the true radiographic density
492 along the ray from the x-ray source to each pixel of each frame of data. The sum of the
493 radiographic density of all the matter penetrated by each pixel's ray is proportional to the
494 logarithm of the bright field for that pixel minus the logarithm of the observation image for that
495 pixel (i.e., log-sub processing).
496
497 3.3.2   Perform distortion correction: The software averages the approximately 30 frames (i.e.,
498 0.5 second of data) to produce a single image and reduces the effect of noise in any individual
499 image. The distortion correction software creates an affine map from each triple of adjacent bead
500 positions in the distortion grid image to the known (true) position of those three beads in the
501 Lucite distortion correction grid. This collection of small affine maps is then used to resample
502 each observed frame of the motion trial into the true coordinates represented by the orthogonal
503 array of beads.
504
505 3.3.3   Apply distortion and non-uniformity corrections to all frames of each trial.
506
507 3.4   Biplane imaging volume calibration.
508
509 NOTE: Image calibration was performed using proprietary software. The software uses a
510 nonlinear optimization algorithm to adjust the observed calibration object bead locations to their
511 known 3D locations. This process is conducted for each set of biplanar calibration images. The
512 result is a system that can digitally project two views of a bone volume and register them against
513 radiographic images of the same bone collected during the data collection.
514
515 3.5   Markerless tracking
516
517 NOTE: Markerless tracking is performed using proprietary software. Software such as Autoscoper
518 and C-Motion can also be used to complete this process.
519
520 3.5.1   On the first frame of the motion trial, rotate and translate the DRR using the software
521 controls until it appears to match well to the biplane x-ray images (**Figure 6**).
522
523 3.5.2   Save the manual solution.
524

525   3.5.3   Apply the optimization algorithm.

526

527   3.5.4   Visually inspect the solution determined to be optimal by the algorithm based on the
528   initial manual solution. If necessary, adjust the solution and repeat steps 3.5.2–3.5.3 until
529   satisfied with the optimized solution.

530

531   3.5.5   Repeat steps 3.5.1–3.5.4 for every 10th frame across the motion trial.

532

533   NOTE: This interval is dependent upon several factors, including frame rate, motion speed, and
534   image quality. Smaller intervals may be required.

535

536   3.5.6   Once every 10th frame is tracked, perform an optimization to create interpolated
537   preliminary solutions that are subsequently optimized.

538

539   3.5.7   Continue to refine the solutions until all the frames of the motion trial are tracked well.

540

541   **4   Data analysis protocol**

542

543   NOTE: The proprietary markerless tracking software used in this protocol results in the raw and
544   filtered trajectories of the anatomical landmarks that will be used to construct anatomical
545   coordinate systems. These coordinates are expressed relative to the laboratory coordinate
546   system defined by the calibration object during the calibration procedure. The following protocol
547   describes, in general terms, the procedures for calculating kinematic outcome measures from
548   these landmark trajectories such that they can be computed in any programming language (e.g.,
549   MATLAB). A second proprietary software is used to calculate kinematics and proximity statistics.

550

551   4.1   Calculate kinematics and proximity statistics

552

553   NOTE: The primary kinematic outcome measures include joint rotations (i.e., Euler angles) and
554   positions. The primary proximity statistics include the minimum gap, average gap, weighted-
555   average contact center, which are calculated for every frame of data. Collectively, these
556   measures describe joint arthrokinematics, or surface interactions during a movement.
557   Anatomical proximities that are aggregated across the motion trial include the average contact
558   center, contact path, and contact path length.

559

560   4.1.1   For each bone and frame of motion, use the filtered anatomical landmark coordinates
561   (i.e., output from the markerless tracking software) to construct a 16-element transformation
562   matrix representing the bone's anatomical coordinate system relative to the laboratory
563   coordinate system.

564

565   4.1.2   Calculate the relative kinematics by relating the anatomical coordinate systems between
566   relevant bones using the software.

567

568   4.1.3   Extract the joint angles and positions using conventional methods[64]. Given the orientation
569   of the anatomical coordinate systems, extract the glenohumeral kinematics using a Z-X'-Y''
570   rotation sequence, extract the scapulothoracic kinematics using a Y-Z'-X'' rotation sequence, and
571   extract the humerothoracic kinematics using a Y-Z'-Y'' rotation sequence.
572
573   4.1.4   Minimum gap: Calculate the smallest gap (i.e., distance) between the centroids of the
574   nearest-neighbor triangle on the opposite bone using the software.
575
576   4.1.5   Average gap: Calculate the area-weighted mean of the minimum gap using the triangles
577   that have the smallest gap to their nearest neighbor within a specified measurement area using
578   the software. Define the measurement area as the triangles closest to the opposite bone whose
579   areas sum to 200 mm^2. Incorporate this measurement area in the calculation to ensure that only
580   the surface that is reasonably near to the opposite bone is included in the average gap
581   calculation.
582
583   NOTE: The sizes of the measurement area (i.e., 200 mm^2) was selected during initial algorithm
584   development after it was found to consistently reflect subacromial space and glenohumeral joint
585   proximities without being overly biased from distant surfaces. Use of this measure for broader
586   surface interactions (e.g., tibiofemoral) may require a larger measurement area.
587
588   4.1.6   Weighted-average contact center (i.e., centroid): Calculate the point on the ROI surface
589   that minimizes the weighted distance to all other triangles within the measurement area (i.e.,
590   triangles closest to the opposite bone whose areas sum to 200 mm^2) using the software. The
591   weighting factor for each triangle in the measurement area is calculated as: triangle area /
592   squared distance to nearest-neighbor centroid (i.e., inverse square weighting). In this way, the
593   triangles that are weighted more heavily are larger (by a factor of 1) and closer to the opposite
594   bone (by a factor of the squared minimum distance).
595
596   4.1.7   Average contact center: Calculate the average position of the contact center (i.e.,
597   centroid) across the motion trial using the software. Given contact centers represent joint
598   arthrokinematics, the average contact center represents the center of surface interactions during
599   a movement.
600
601   4.1.8   Contact path: Define by connecting the coordinates of the weighted-average contact
602   center across the motion trial using the software.
603
604   4.1.9   Contact path length: Calculate the length of the contact path across the motion trial using
605   the software.
606
607   **REPRESENTATIVE RESULTS:**
608   A 52-year-old asymptomatic female (BMI = 23.6 kg/m^2) was recruited as part of a previous
609   investigation and underwent motion testing (coronal plane abduction) on her dominant (right)
610   shoulder[65]. Prior to data collection, the participant provided written informed consent. The
611   investigation was approved by Henry Ford Health System's Institutional Review Board. Data

612   collection was performed using the protocol previously described (**Figure 3**).

614   The participant's glenohumeral, scapulothoracic, and humerothoracic kinematics are presented
615   in **Figure 7**, **Figure 8**, and **Figure 9**, respectively. Visual inspection of glenohumeral and
616   scapulothoracic kinematics suggests the participant's shoulder motion was consistent with what
617   is generally expected during coronal plane abduction[66]. Specifically, glenohumeral motion
618   consisted of elevation and slight external rotation, and was generally in a plane posterior to the
619   scapula (**Figure 7**), while scapulothoracic motion consisted of upward rotation, posterior tilt, and
620   slight internal/external rotation (**Figure 8**).

622   During the motion trial, the minimum subacromial distance (i.e., narrowest width of the
623   subacromial outlet for a given frame) ranged from 1.8 mm at 74.0° humerothoracic elevation
624   (frame 45) to 8.3 mm at 134.0° humerothoracic elevation (frame 89) (**Figure 10A, Figure 11A**).
625   The average subacromial distance (i.e., average width of the subacromial outlet within the
626   specified 200 mm^2 measurement area) tended to follow a similar trajectory as the minimum
627   distance metric. For example, the average subacromial distance ranged from 4.2 mm at 75.4°
628   humerothoracic elevation (frame 46) to 9.2 mm at 134.0° humerothoracic elevation (frame 89).
629   Finally, the minimum subacromial distance tended to follow a complementary trajectory to the
630   surface area metric (**Figure 10B**) such that the minimum distance tended to be smaller when the
631   surface area is larger. Plotting the location of the minimum distance on the humeral head
632   suggests the location closest to the acromion shifts laterally across the rotator cuff footprint as
633   the humerothoracic elevation angle increases (**Figure 11A**). Across the motion trial, the contact
634   path length measured 40.5 mm on the humeral head and 28.8 mm on the acromion.

636   During the motion trial, the minimum glenohumeral distance (i.e., narrowest width of the
637   glenohumeral joint space) ranged from 1.0 mm at 137.9° humerothoracic elevation (frame 92)
638   to 2.1 mm at 34.2° humerothoracic elevation (frame 21) (**Figure 12A, Figure 11B**). As with the
639   subacromial distances, the average glenohumeral distance tended to follow a similar trajectory
640   as the minimum distance metric, and these distances followed a complementary trajectory with
641   the surface area metric (**Figure 12B**). For example, the average glenohumeral distance ranged
642   from 1.4 mm at 137.9° humerothoracic elevation (frame 92) to 2.6 mm at 23.5° humerothoracic
643   elevation (frame 12). Plotting the location of the glenohumeral contact center relative to the
644   glenoid edge contours suggest that the participant's arthrokinematics included moderate surface
645   interactions. Specifically, the humerus stayed relatively centered in the glenoid in the
646   anterior/posterior direction but shifted superiorly and then inferiorly during the motion trial
647   (**Figure 11B**). Across the motion trial, the contact path length measured 30.0 mm on the glenoid
648   and 45.4 mm on the humeral head.

650   **FIGURE AND TABLE LEGENDS:**

652   **Figure 1: The CT field of view**. (**A**) coronal, (**B**) sagittal, and (**C**) transverse planes. During
653   acquisition, the CT technologist ensures the field of view includes the clavicle (superiorly), the
654   distal humeral epicondyles (inferiorly), the entire glenohumeral joint (laterally), and the
655   costovertebral and sternocostal joints (medially).

656

Figure 2: Schematic of the biplane videoradiographic system. The x-ray systems are positioned with a 50° inter-beam angle and a source-to-image distance (SID) of 183 cm. Participants are positioned in the biplane volume such that their glenohumeral joint is located approximately at the intersection of the x-ray beams. Systems are termed "green" and "red" to distinguish the control panels and the filenames of the images.

Figure 3: Biplane radiographic images from a representative subject during coronal plane abduction. Although the jaw appears in the images of the green system, care should be taken to avoid including the head in the field of view to minimize dose to this area.

Figure 4: Definition of anatomical coordinate systems. (**A**) Humeral coordinate system defined by digitizing the geometric center of the humeral head, medial epicondyle, and lateral epicondyle. (**B**) Scapular coordinate system defined by digitizing the medial spine, inferior angle, and posterior aspect of the acromioclavicular joint. (**C**) Rib coordinate system defined by digitizing the posterior aspect of the costovertebral facet, the lateral-most aspect of the rib, and the lateral sternum at the level of the rib.

Figure 5: Definition of regions of interest (ROI) for proximity statistics. (**A**) humeral head ROI, which is used to calculate acromiohumeral distance and glenohumeral joint contact patterns, (**B**) acromial and glenoid ROIs, which are used to calculate acromiohumeral distance and glenohumeral joint contact patterns, respectively.

Figure 6: Screenshots of the proprietary markerless tracking software. The screenshot illustrates the optimized solutions of the humerus and scapula from a representative subject during coronal plane abduction.

Figure 7: Glenohumeral kinematics from a representative subject during a single trial of coronal plane abduction. Note: Anterior position has been transformed to be a positive value. Abbreviations: med. = medial; lat. = lateral; sup. = superior; inf. = inferior; ant. = anterior; post. = posterior.

Figure 8: Scapulothoracic kinematics from a representative subject during a single trial of coronal plane abduction. Note: Anterior position has been transformed to be a positive value. Abbreviations: IR = internal rotation; ER = external rotation; UR = upward rotation; DR = downward rotation; AT = anterior tilt; PT = posterior tilt; med. = medial; lat. = lateral; sup. = superior; inf. = inferior; ant. = anterior; post. = posterior.

Figure 9: Humerothoracic kinematics from a representative subject during a single trial of coronal plane abduction. Note: Anterior position has been transformed to be a positive value. Abbreviations: med. = medial; lat. = lateral; sup. = superior; inf. = inferior; ant. = anterior; post. = posterior.

699 **Figure 10: Assessment of the subacromial space during a trial of coronal plane abduction in a**
700 **representative subject**. (**A**) Measures of acromiohumeral distance are displayed across frames
701 along with the corresponding humerothoracic elevation angles. The minimum distance is
702 calculated as the smallest distance between the centroids of the nearest-neighbor triangle
703 between the humeral head and acromial ROIs. The average distance represents the area-
704 weighted mean of the minimum distance, calculated over the triangles in the humeral head ROI
705 that have the smallest gap to their nearest neighbor on the acromial ROI. (**B**) The surface area of
706 the humeral head ROI that is within 10 mm of the acromial ROI is displayed across frames along
707 with the corresponding humerothoracic elevation angles. Abbreviation: HT = humerothoracic.

709 **Figure 11: Proximity mapping**. (**A**) subacromial space, (**B**) glenohumeral joint space. The
710 subacromial proximity is mapped on the humeral head ROI using the minimum distance metric
711 for the frame of data in which the minimum distance was smallest (i.e., frame #45). The contact
712 path (black) represents the minimum distance trajectory between frames #1–45. The
713 glenohumeral joint proximity is mapped using the weighted-average contact center for the frame
714 of data in which the joint space was smallest (i.e., frame #92). The contact path (black) represents
715 the centroid trajectory between frames #1–92.

717 **Figure 12: Assessment of the glenohumeral joint space during a trial of coronal plane abduction**
718 **in a representative subject**. (**A**) Measures of glenohumeral joint space are displayed across
719 frames along with the corresponding humerothoracic elevation angles. The minimum distance is
720 calculated as the smallest distance between the centroids of the nearest-neighbor triangle
721 between the glenoid and humeral head ROIs. The average distance represents the area-weighted
722 mean of the minimum distance, calculated over the triangles in the glenoid ROI that have the
723 smallest gap to their nearest neighbor on the humeral head ROI. (**B**) The surface area of the
724 glenoid ROI that is within 10 mm of the humeral head ROI is displayed across frames along with
725 the corresponding humerothoracic elevation angles. Abbreviation: HT = humerothoracic.

727 **DISCUSSION:**
728 The technique described here overcomes several disadvantages associated with conventional
729 techniques for assessing shoulder motion (i.e., cadaveric simulations, 2D imaging, static 3D
730 imaging, video-based motion capture systems, wearable sensors, etc.) by providing accurate
731 measures of 3D joint motion during dynamic activities. The accuracy of the protocol described
732 herein was established for the glenohumeral joint against the gold standard of radiostereometric
733 analysis (RSA) to be ±0.5° and ±0.4 mm[67,68]. Similar protocols have been developed for other
734 joints such as the knee[69], spine[70], and foot/ankle[71]. Importantly, without a system that is
735 sufficiently accurate, the sample size necessary to detect statistically significant and clinically
736 potential meaningful differences in joint motion could be prohibitive. Furthermore, this level of
737 accuracy affords the ability to describe potentially important outcome measures such as joint
738 positions and/or translations[62,72], arthrokinematics[72–75], subacromial distances[61,72,75], and
739 instantaneous axes of motion[76]. Ultimately, accurately measuring in-vivo joint motion is essential
740 for providing a mechanistic understanding of shoulder function under normal and pathologic
741 conditions, and for assessing the effects of non-surgical and surgical clinical interventions.

743   The accuracy afforded by quantifying shoulder kinematics using biplane videoradiography comes
744   with many challenges and limitations. The primary limitation associated with this technique is
745   the radiation exposure to the participant as a result of the CT scan and biplane x-ray imaging.
746   Consequently, the number of motion trials that can be acquired or follow-up sessions over time
747   is limited. The effective dose corresponding with the protocol described here is approximately
748   10.5 mSv, with the majority (approximately 10 mSv) coming from the CT scan, which includes
749   imaging of the distal humerus so that the epicondyles can be used to construct the humeral
750   anatomical coordinate system[64]. For context, this dose corresponds to approximately 3 years of
751   exposure to natural background sources of radiation. Recent recommendations of the National
752   Council on Radiation Protection and Measurements suggest this dose can be classified as "minor"
753   assuming a moderate expected benefit to the individual or society[77]. Consequently, it is
754   imperative that motion analysis using biplane videoradiography be used in a well-designed study
755   based on a solid scientific premise that has the potential to have an significant impact on public
756   health.
757
758   Reducing the dose associated with biplane videoradiography is crucial to facilitate the broader
759   use of this technology in research and clinical settings. Fortunately, recent advances in CT and
760   MR imaging may substantially reduce the dose to the participant. For example, humeral and
761   scapular bone models derived using MRI[78,79] or lower dose CT[80] have been shown to have
762   acceptable accuracy for many research applications. Furthermore, redefining the humeral
763   coordinate system in a manner that does not require the humeral epicondyles[81] will decrease the
764   dose by reducing the CT imaging volume. Careful practice of motion trials before acquiring any
765   images is also crucial to ensure that each collected trial has value and does not unnecessarily add
766   to the participant's total dose. Ultimately, carefully considering these factors, and many others,
767   is critical when responsibly using biplane videoradiography to quantify 3D kinematics in human
768   research participants.
769
770   The participant's body habitus and differences in tissue density (and therefore image brightness)
771   between the central torso and the lateral aspect of the shoulder presents additional challenges
772   when quantifying shoulder motion using biplane videoradiography. In particular, clear
773   visualization of the scapula and ribs is often challenging using the radiographic technique
774   described in this protocol (i.e., ~70 kVp, 320 mA, 2 ms pulsed exposure) in individuals with high
775   BMI (>30 kg/m^2) and women with large or dense breast tissue. Kinematic tracking accuracy likely
776   deteriorates without clear visualization of bone edges. Consequently, careful selection of
777   participants by restricting BMI can ameliorate many of these challenging imaging considerations.
778   However, "washout" of the lateral acromion at lower angles of humeral elevation is common
779   even in participants of healthy body habitus (**Figure 2A**, green system at Frame 1). This is because
780   there is little tissue (and thus density) around the acromion when the humerus is at lower angles
781   of elevation, and visibility of this region is conceded in order to visualize the scapula and ribs.
782   However, once the humerus elevates and the bulk of the shoulder in projected onto itself (thus
783   increasing radiographic density), the acromion becomes well-visualized. Therefore, the optimal
784   radiographic technique for a motion trial does not necessarily guarantee visualization of all bones
785   at all times, but allows for the clear visualization of enough bony anatomy to conduct markerless
786   tracking.

787
788   Another challenge when using biplane videoradiography is the relatively small 3D imaging
789   volume, which is predominantly defined by the image receptor size, the orientation of the two
790   imaging systems, and the SID. Although limiting the 3D imaging volume helps control the
791   radiation dose (i.e., through collimation), a small imaging volume may restrict the range over
792   which joint motion can be acquired and/or the types of tasks being assessed. For example, tasks
793   that require trunk motion (e.g., throwing) may be incompatible with biplane videoradiography
794   motion analysis because the participant will likely move outside of the 3D imaging volume while
795   performing the task. Patient movement outside the imaging volume is common even in simpler
796   tasks such as raising the arm, especially in individuals whose humeral elevation range of motion
797   is significantly impaired (e.g., due to massive rotator cuff tears, adhesive capsulitis, OA), because
798   these individuals often compensate by leaning to the contralateral side. Consequently, careful
799   positioning of the participant within the imaging volume and verbal cues to avoid leaning are
800   crucial steps in the data collection process (section 2.4).
801
802   The small 3D imaging volume also limits the visualization of other segments that may be of
803   interest. For example, tracking the torso is necessary to quantify scapulothoracic and
804   humerothoracic kinematics. The protocol described in this article addresses this challenge by
805   tracking the third and fourth ribs. However, other investigators have tracked the torso using an
806   external surface-based tracking system synced with the radiographic system[49,50,62]. Each of these
807   approaches has unique limitations. For example, tracking the ribs requires good visualization of
808   the central torso, which is challenging in individuals with larger body habitus without washing
809   out the lateral shoulder, as previously described. Furthermore, tracking the ribs may be
810   challenging with a smaller image intensifier (i.e., less than 40 cm). In contrast, tracking torso
811   motion using surface sensors introduces skin motion artifact. Regardless of the approach used,
812   the limited 3D imaging volume remains a challenge when quantifying shoulder kinematics using
813   biplane videoradiography.
814
815   In summary, biplane videoradiography allows for highly accurate quantification of shoulder
816   kinematics. Variations in the protocol described herein has been used for numerous studies
817   within the lab[58,59,72,73,82], with each protocol variation carefully constructed based on the specific
818   research aims in order to minimize dose, maximize image quality, and maximize segment
819   visibility. Ultimately, accurately measuring in-vivo joint motion is important for providing a
820   mechanistic understanding of shoulder function under normal and pathologic conditions, and for
821   assessing the effects of non-surgical and surgical clinical interventions.
822

828
829   **DISCLOSURES:**
830   The authors have no conflicts of interest.

831
832 **REFERENCES:**
833 1. Milgrom, C., Schaffler, M., Gilbert, S. van Holsbeeck, M. Rotator-cuff changes in
834 asymptomatic adults. The effect of age, hand dominance and gender. *Journal of Bone and Joint*
835 *Surgery (British Volume)*. **77** (2), 296–298 (1995).
836 2. Kim, H. M. et al. Location and initiation of degenerative rotator cuff tears: an analysis of
837 three hundred and sixty shoulders. *Journal of Bone and Joint Surgery (American Volume)*. **92** (5),
838 1088–1096 (2010).
839 3. Yamamoto, A. et al. Prevalence and risk factors of a rotator cuff tear in the general
840 population. *Journal of Shoulder and Elbow Surgery*. **19** (1), 116–120 (2010).
841 4. Colvin, A. C., Egorova, N., Harrison, A. K., Moskowitz, A., Flatow, E. L. National trends in
842 rotator cuff repair. *Journal of Bone and Joint Surgery (American Volume)*. **94** (3), 227–233 (2012).
843 5. Vitale, M. A. et al. Rotator cuff repair: an analysis of utility scores and cost-effectiveness.
844 *Journal of Shoulder and Elbow Surgery*. **16** (2), 181–187 (2007).
845 6. Zacchilli, M. A., Owens, B. D. Epidemiology of shoulder dislocations presenting to
846 emergency departments in the United States. *Journal of Bone and Joint Surgery (American*
847 *Volume)*. **92** (3), 542–549 (2010).
848 7. Oh, J. H. et al. The prevalence of shoulder osteoarthritis in the elderly Korean population:
849 association with risk factors and function. *Journal of Shoulder and Elbow Surgery*. **20** (5), 756–763
850 (2011).
851 8. Kobayashi, T. et al. Prevalence of and risk factors for shoulder osteoarthritis in Japanese
852 middle-aged and elderly populations. *Journal of Shoulder and Elbow Surgery*. **23** (5), 613–619
853 (2014).
854 9. Ludewig, P.M., Reynolds, J. F. The association of scapular kinematics and glenohumeral
855 joint pathologies. *Journal of Orthopaedic and Sports Physical Therapy*. **39** (2), 90–104 (2009).
856 10. Michener, L. A., McClure, P. W., Karduna, A. R. Anatomical and biomechanical
857 mechanisms of subacromial impingement syndrome. *Clinical Biomechanics (Bristol, Avon)*. **18** (5),
858 369–379 (2003).
859 11. Seitz, A. L., McClure, P. W., Finucane, S., Boardman, N. D., Michener, L. A. Mechanisms of
860 rotator cuff tendinopathy: intrinsic, extrinsic, or both? *Clinical Biomechanics (Bristol, Avon)*. **26**
861 (1), 1–12 (2011).
862 12. Lawrence, R. L., Braman, J. P., Ludewig, P. M. Shoulder kinematics impact subacromial
863 proximities: a review of the literature. *Brazilian Journal of Physical Therapy*. **24** (3), 219–230
864 (2019).
865 13. McClure, P. W., Michener, L. A., Karduna, A. R. Shoulder function and 3-dimensional
866 scapular kinematics in people with and without shoulder impingement syndrome. *Physical*
867 *Therapy*. **86** (8), 1075–1090 (2006).
868 14. Rundquist, P. J. Alterations in scapular kinematics in subjects with idiopathic loss of
869 shoulder range of motion. *Journal of Orthopaedic and Sports Physical Therapy*. **37** (1), 19–25
870 (2007).
871 15. Graichen, H. et al. Effect of abducting and adducting muscle activity on glenohumeral
872 translation, scapular kinematics and subacromial space width in vivo. *Journal of Biomechanics*.
873 **38** (4), 755–760 (2005).
874 16. Bey, M. J., Kline, S. K., Zauel, R., Lock, T. R., Kolowich, P. A. Measuring dynamic in-vivo

875 glenohumeral joint kinematics: technique and preliminary results. *Journal of Biomechanics*. **41**
876 (3), 711–714 (2008).
877 17. Poppen, N. K., Walker, P. S. Normal and abnormal motion of the shoulder. *Journal of Bone*
878 *and Joint Surgery (American Volume)*. **58** (2), 195–201 (1976).
879 18. Graichen, H. et al. Magnetic resonance-based motion analysis of the shoulder during
880 elevation. *Clinical Orthopaedics and Related Research*. (370), 154–163 (2000).
881 19. Howell, S. M., Galinat, B. J., Renzi, A. J., Marone, P. J. Normal and abnormal mechanics of
882 the glenohumeral joint in the horizontal plane. *Journal of Bone and Joint Surgery (American*
883 *Volume)*. **70** (2), 227–232 (1988).
884 20. Bergmann, G. et al. In vivo glenohumeral contact forces--measurements in the first
885 patient 7 months postoperatively. *Journal of Biomechanics*. **40** (10), 2139–2149 (2007).
886 21. Westerhoff, P. et al. In vivo measurement of shoulder joint loads during activities of daily
887 living. *Journal of Biomechanics*. **42** (12), 1840–1849 (2009).
888 22. Bergmann, G. et al. In vivo gleno-humeral joint loads during forward flexion and
889 abduction. *Journal of Biomechanics*. **44** (8), 1543–1552 (2011).
890 23. Halder, A. M., Zhao, K. D., Odriscoll, S. W., Morrey, B. F., An, K. N. Dynamic contributions
891 to superior shoulder stability. *Journal of Orthopaedic Research*. **19** (2), 206–212 (2001).
892 24. Debski, R. E. et al. A new dynamic testing apparatus to study glenohumeral joint motion.
893 *Journal of Biomechanics*. **28** (7), 869–874 (1995).
894 25. Malicky, D. M., Soslowsky, L. J., Blasier, R. B., Shyr, Y. Anterior glenohumeral stabilization
895 factors: progressive effects in a biomechanical model. *Journal of Orthopaedic Research*. **14** (2),
896 282–288 (1996).
897 26. Payne, L. Z., Deng, X. H., Craig, E. V., Torzilli, P. A., Warren, R. F. The combined dynamic
898 and static contributions to subacromial impingement. A biomechanical analysis. *American*
899 *Journal of Sports Medicine*. **25** (6), 801–808 (1997).
900 27. Wuelker, N., Wirth, C. J., Plitz, W., Roetman, B. A dynamic shoulder model: reliability
901 testing and muscle force study. *Journal of Biomechanics*. **28** (5), 489–499 (1995).
902 28. Dillman, C. J., Fleisig, G. S., Andrews, J. R. Biomechanics of pitching with emphasis upon
903 shoulder kinematics. *Journal of Orthopaedic and Sports Physical Therapy*. **18** (2), 402–408 (1993).
904 29. Fleisig, G. S., Andrews, J. R., Dillman, C. J., Escamilla, R. F. Kinetics of baseball pitching with
905 implications about injury mechanisms. *American Journal of Sports Medicine*. **23** (2), 233–239
906 (1995).
907 30. Fleisig, G. S., Barrentine, S. W., Zheng, N., Escamilla, R. F., Andrews, J. R. Kinematic and
908 kinetic comparison of baseball pitching among various levels of development. *Journal of*
909 *Biomechanics*. **32** (12), 1371–1375 (1999).
910 31. Werner, S. L., Gill, T. J., Murray, T. A., Cook, T. D., Hawkins, R. J. Relationships between
911 throwing mechanics and shoulder distraction in professional baseball pitchers. *American Journal*
912 *of Sports Medicine*. **29** (3), 354–358 (2001).
913 32. An, K. N., Browne, A. O., Korinek, S., Tanaka, S., Morrey, B. F. Three-dimensional
914 kinematics of glenohumeral elevation. *Journal of Orthopaedic Research*. **9** (1), 143–149 (1991).
915 33. Johnson, M. P., McClure, P. W., Karduna, A. R. New method to assess scapular upward
916 rotation in subjects with shoulder pathology. *Journal of Orthopaedic and Sports Physical Therapy*.
917 **31** (2), 81–89 (2001).
918 34. Borstad, J. D., Ludewig, P. M. Comparison of scapular kinematics between elevation and

919 lowering of the arm in the scapular plane. *Clinical Biomechanics (Bristol, Avon)*. **17** (9–10), 650–
920 659 (2002).

35.   Meskers, C. G., van der Helm, F. C., Rozendaal, L. A., Rozing, P. M. In vivo estimation of
922 the glenohumeral joint rotation center from scapular bony landmarks by linear regression.
923 *Journal of Biomechanics*. **31** (1), 93–96 (1998).

36.   McClure, P. W., Michener, L. A., Sennett, B. J., Karduna, A. R. Direct 3-dimensional
925 measurement of scapular kinematics during dynamic movements in vivo. *Journal of Shoulder and
926 Elbow Surgery*. **10** (3), 269–277 (2001).

37.   Lawrence, R. L., Braman, J. P., LaPrade, R. F., Ludewig, P.M. Comparison of 3-dimensional
928 shoulder complex kinematics in individuals with and without shoulder pain, part 1:
929 sternoclavicular, acromioclavicular, and scapulothoracic joints. *Journal of Orthopaedic and Sports
930 Physical Therapy*. **44** (9), 636–645, A631–638 (2014).

38.   Lawrence, R. L., Braman, J. P., Staker, J. L., LaPrade, R. F., Ludewig, P. M. Comparison of
932 3-dimensional shoulder complex kinematics in individuals with and without shoulder pain, part
933 2: glenohumeral joint. *Journal of Orthopaedic and Sports Physical Therapy*. **44** (9), 646–655,
934 B641–643 (2014).

39.   Burkhart, S. S. Fluoroscopic comparison of kinematic patterns in massive rotator cuff
936 tears. A suspension bridge model. *Clinical Orthopaedics and Related Research*. **284**, 144–152
937 (1992).

40.   Mandalidis, D. G., Mc Glone, B. S., Quigley, R. F., McInerney, D., O'Brien, M. Digital
939 fluoroscopic assessment of the scapulohumeral rhythm. *Surgical and Radiologic Anatomy*. **21** (4),
940 241–246 (1999).

41.   Pfirrmann, C. W., Huser, M., Szekely, G., Hodler, J., Gerber, C. Evaluation of complex joint
942 motion with computer-based analysis of fluoroscopic sequences. *Investigative Radiology*. **37** (2),
943 73–76 (2002).

42.   Deutsch, A., Altchek, D. W., Schwartz, E., Otis, J. C., Warren, R. F. Radiologic measurement
945 of superior displacement of the humeral head in the impingement syndrome. *Journal of Shoulder
946 and Elbow Surgery*. **5** (3), 186–193 (1996).

43.   Hawkins, R. J., Schutte, J. P., Janda, D. H., Huckell, G. H. Translation of the glenohumeral
948 joint with the patient under anesthesia. *Journal of Shoulder and Elbow Surgery*. **5** (4), 286–292
949 (1996).

44.   Yamaguchi, K. et al*. Glenohumeral motion in patients with rotator cuff tears: a
951 comparison of asymptomatic and symptomatic shoulders. *Journal of Shoulder and Elbow Surgery*.
952 **9** (1), 6–11 (2000).

45.   Paletta, G. A. Jr., Warner, J. J., Warren, R. F., Deutsch, A., Altchek, D. W. Shoulder
954 kinematics with two-plane x-ray evaluation in patients with anterior instability or rotator cuff
955 tearing. *Journal of Shoulder and Elbow Surgery*. **6** (6), 516–527 (1997).

46.   Graichen, H. et al*. Three-dimensional analysis of the width of the subacromial space in
957 healthy subjects and patients with impingement syndrome. *AJR: American Journal of
958 Roentgenology*. **172** (4), 1081–1086 (1999).

47.   Rhoad, R. C. et al*. A new in vivo technique for three-dimensional shoulder kinematics
960 analysis. *Skeletal Radiology*. **27** (2), 92–97 (1998).

48.   Baeyens, J. P., Van Roy, P., De Schepper, A., Declercq, G., Clarijs, J. P. Glenohumeral joint
962 kinematics related to minor anterior instability of the shoulder at the end of the late preparatory

963 phase of throwing. *Clinical Biomechanics (Bristol, Avon)*. **16** (9), 752–757 (2001).

964 49. Lawrence, R. L., Braman, J. P., Keefe, D. F., Ludewig, P. M. The Coupled Kinematics of
965 Scapulothoracic Upward Rotation. *Physical Therapy*. **100** (2), 283–294 (2020).

966 50. Lawrence, R. L., Braman, J. P., Ludewig, P. M. The impact of decreased scapulothoracic
967 upward rotation on subacromial proximities. *Journal of Orthopaedic and Sports Physical Therapy*.
968 **49** (3), 180–191 (2019).

969 51. Matsuki, K. et al. Dynamic in vivo glenohumeral kinematics during scapular plane
970 abduction in healthy shoulders. *Journal of Orthopaedic and Sports Physical Therapy*. **42** (2), 96–
971 104 (2012).

972 52. Chapman, R. M., Torchia, M. T., Bell, J. E., Van Citters, D. W. Assessing shoulder
973 biomechanics of healthy elderly individuals during activities of daily living using inertial
974 measurement units: High maximum elevation Is achievable but rarely used. *Journal of*
975 *Biomechanical Engineering*. **141** (4) (2019).

976 53. De Baets, L., van der Straaten, R., Matheve, T.,Timmermans, A. Shoulder assessment
977 according to the international classification of functioning by means of inertial sensor
978 technologies: A systematic review. *Gait and Posture*. **57**, 278–294 (2017).

979 54. Dowling, B., McNally, M. P., Laughlin, W. A., Onate, J. A. Changes in throwing arm
980 mechanics at increased throwing distances during structured long-toss. *American Journal of*
981 *Sports Medicine*. **46** (12), 3002–3006 (2018).

982 55. Kirking, B., El-Gohary, M., Kwon, Y. The feasibility of shoulder motion tracking during
983 activities of daily living using inertial measurement units. *Gait and Posture*. **49**, 47–53 (2016).

984 56. Morrow, M. M. B., Lowndes, B., Fortune, E., Kaufman, K. R., Hallbeck, M. S. Validation of
985 inertial measurement units for upper body kinematics. *Journal of Applied Biomechanics*. **33** (3),
986 227–232 (2017).

987 57. Rawashdeh, S. A., Rafeldt, D. A., Uhl, T. L. Wearable IMU for shoulder injury prevention in
988 overhead sports. *Sensors (Basel)*. **16** (11) (2016).

989 58. Baumer, T. G. et al. Effects of asymptomatic rotator cuff pathology on in vivo shoulder
990 motion and clinical outcomes. *Journal of Shoulder and Elbow Surgery*. **26** (6), 1064–1072 (2017).

991 59. Bey, M. J. et al. In vivo measurement of subacromial space width during shoulder
992 elevation: technique and preliminary results in patients following unilateral rotator cuff repair.
993 *Clinical Biomechanics (Bristol, Avon)*. **22** (7), 767–773 (2007).

994 60. Peltz, C. D. et al. Differences in glenohumeral joint morphology between patients with
995 anterior shoulder instability and healthy, uninjured volunteers. *Journal of Shoulder and Elbow*
996 *Surgery*. **24** (7), 1014–1020 (2015).

997 61. Coats-Thomas, M. S., Massimini, D. F., Warner, J. J. P., Seitz, A. L. In vivo evaluation of
998 subacromial and internal impingement risk in asymptomatic individuals. *American Journal of*
999 *Physical Medicine and Rehabilitation*. **97** (9), 659–665 (2018).

1000 62. Millett, P. J., Giphart, J. E., Wilson, K. J., Kagnes, K., Greenspoon, J. A. Alterations in
1001 glenohumeral kinematics in patients with rotator cuff tears measured with biplane fluoroscopy.
1002 *Arthroscopy*. **32** (3), 446–451 (2016).

1003 63. Li, W., Hou, Q. Analysis and correction of the nonuniformity of light field in the high
1004 resolution X-ray digital radiography. *Sixth International Conference on Natural Computation.* **7**,
1005 3803–3807 (2010).

1006 64. Wu, G. et al. ISB recommendation on definitions of joint coordinate systems of various

1007 joints for the reporting of human joint motion--Part II: shoulder, elbow, wrist and hand. *Journal*
1008 *of Biomechanics*. **38** (5), 981–992 (2005).

1009 65.   Baumer, T. G. et al. Effects of rotator cuff pathology and physical therapy on in vivo
1010 shoulder motion and clinical outcomes in patients with a symptomatic full-thickness rotator cuff
1011 tear. *Orthopaedic Journal of Sports Medicine*. **4** (9), 2325967116666506 (2016).

1012 66.   Ludewig, P. M. et al. Motion of the shoulder complex during multiplanar humeral
1013 elevation. *Journal of Bone and Joint Surgery (American Volume)*. **91** (2), 378–389 (2009).

1014 67.   Bey, M. J., Zauel, R., Brock, S. K., Tashman, S. Validation of a new model-based tracking
1015 technique for measuring three-dimensional, in vivo glenohumeral joint kinematics. *Journal of*
1016 *Biomechanical Engineering*. **128** (4), 604–609 (2006).

1017 68.   Tashman, S., Anderst, W. In-vivo measurement of dynamic joint motion using high speed
1018 biplane radiography and CT: application to canine ACL deficiency. *Journal of Biomechanical*
1019 *Engineering*. **125** (2), 238–245 (2003).

1020 69.   Anderst, W., Zauel, R., Bishop, J., Demps, E., Tashman, S. Validation of three-dimensional
1021 model-based tibio-femoral tracking during running. *Medical Engineering and Physics*. **31** (1), 10–
1022 16 (2009).

1023 70.   Kage, C. C. et al. Validation of an automated shape-matching algorithm for biplane
1024 radiographic spine osteokinematics and radiostereometric analysis error quantification. *PloS*
1025 *One*. **15** (2), e0228594 (2020).

1026 71.   Pitcairn, S., Kromka, J., Hogan, M., Anderst, W. Validation and application of dynamic
1027 biplane radiography to study in vivo ankle joint kinematics during high-demand activities. *Journal*
1028 *of Biomechanics*. **103**, 109696 (2020).

1029 72.   Bey, M. J. et al. In vivo shoulder function after surgical repair of a torn rotator cuff:
1030 glenohumeral joint mechanics, shoulder strength, clinical outcomes, and their interaction.
1031 *American Journal of Sports Medicine*. **39** (10), 2117–2129 (2011).

1032 73.   Peltz, C. D. et al. Associations between in-vivo glenohumeral joint motion and
1033 morphology. *Journal of Biomechanics*. **48** (12), 3252–3257 (2015).

1034 74.   Massimini, D. F., Warner, J. J., Li, G. Glenohumeral joint cartilage contact in the healthy
1035 adult during scapular plane elevation depression with external humeral rotation. *Journal of*
1036 *Biomechanics*. **47** (12), 3100–3106 (2014).

1037 75.   Miller, R. M. et al. Effects of exercise therapy for the treatment of symptomatic full-
1038 thickness supraspinatus tears on in vivo glenohumeral kinematics. *Journal of Shoulder and Elbow*
1039 *Surgery*. **25** (4), 641–649 (2016).

1040 76.   Lawrence, R. L., Ruder, M. C., Zauel, R., Bey, M. J. Instantaneous helical axis estimation of
1041 glenohumeral kinematics: The impact of rotator cuff pathology. *Journal of Biomechanics*. **109**
1042 109924 (2020).

1043 77.   National Council on Radiation Protection and Measurements. *Evaluating and*
1044 *communicating radiation risks for studies involving human subjects: guidance for researchers and*
1045 *institutional review boards: recommendations of the National Council on Radiation Protection*
1046 *and Measurements*. National Council on Radiation Protection and Measurements (2020).

1047 78.   Akbari-Shandiz, M. et al. MRI vs CT-based 2D-3D auto-registration accuracy for
1048 quantifying shoulder motion using biplane video-radiography. *Journal of Biomechanics*. **82**
1049 30385001 (2019).

1050 79.   Breighner, R. E. et al. Technical developments: Zero echo time imaging of the shoulder:

1051 enhanced osseous detail by using MR imaging. *Radiology*. **286** (3), 960–966 (2018).

1052 80. Fox, A. M. et al. The effect of decreasing computed tomography dosage on
1053 radiostereometric analysis (RSA) accuracy at the glenohumeral joint. *Journal of Biomechanics*. **44**
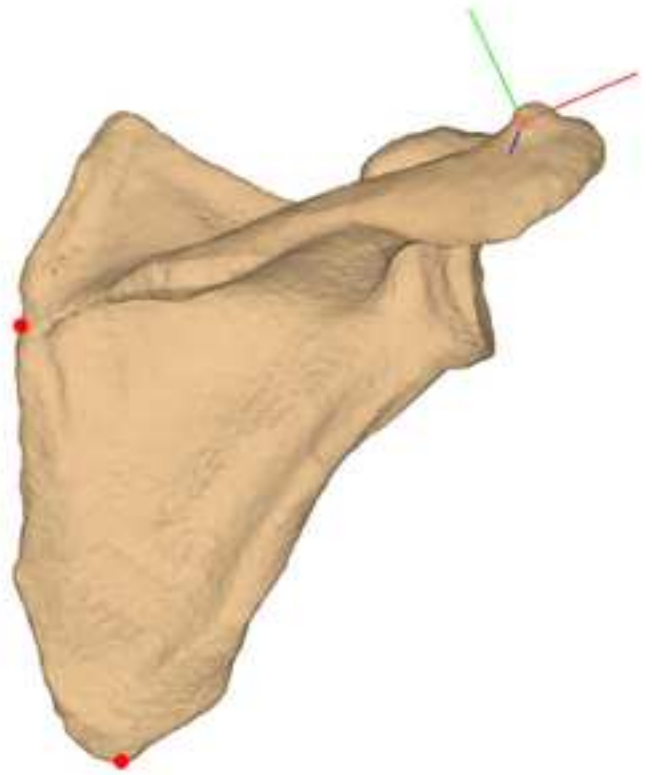1054 (16), 2847–2850 (2011).

1055 81. Lawrence, R. L. et al. Effect of glenohumeral elevation on subacromial supraspinatus
1056 compression risk during simulated reaching. *Journal of Orthopaedic Research*. **35** (10), 2329–
1057 2337 (2017).

1058 82. Peltz, C. D. et al. Associations among shoulder strength, glenohumeral joint motion, and
1059 clinical outcome after rotator cuff repair. *American Journal of Orthopedics (Belle Mead, N.J.)*. **43**
1060 (5), 220–226 (2014).

1061

Figure1

Figure2

Red image intensifier

Green x-ray source

50°

Green image intensifier

SID = 183 cm

Red x-ray source

Figure3

Figure4

Figure5
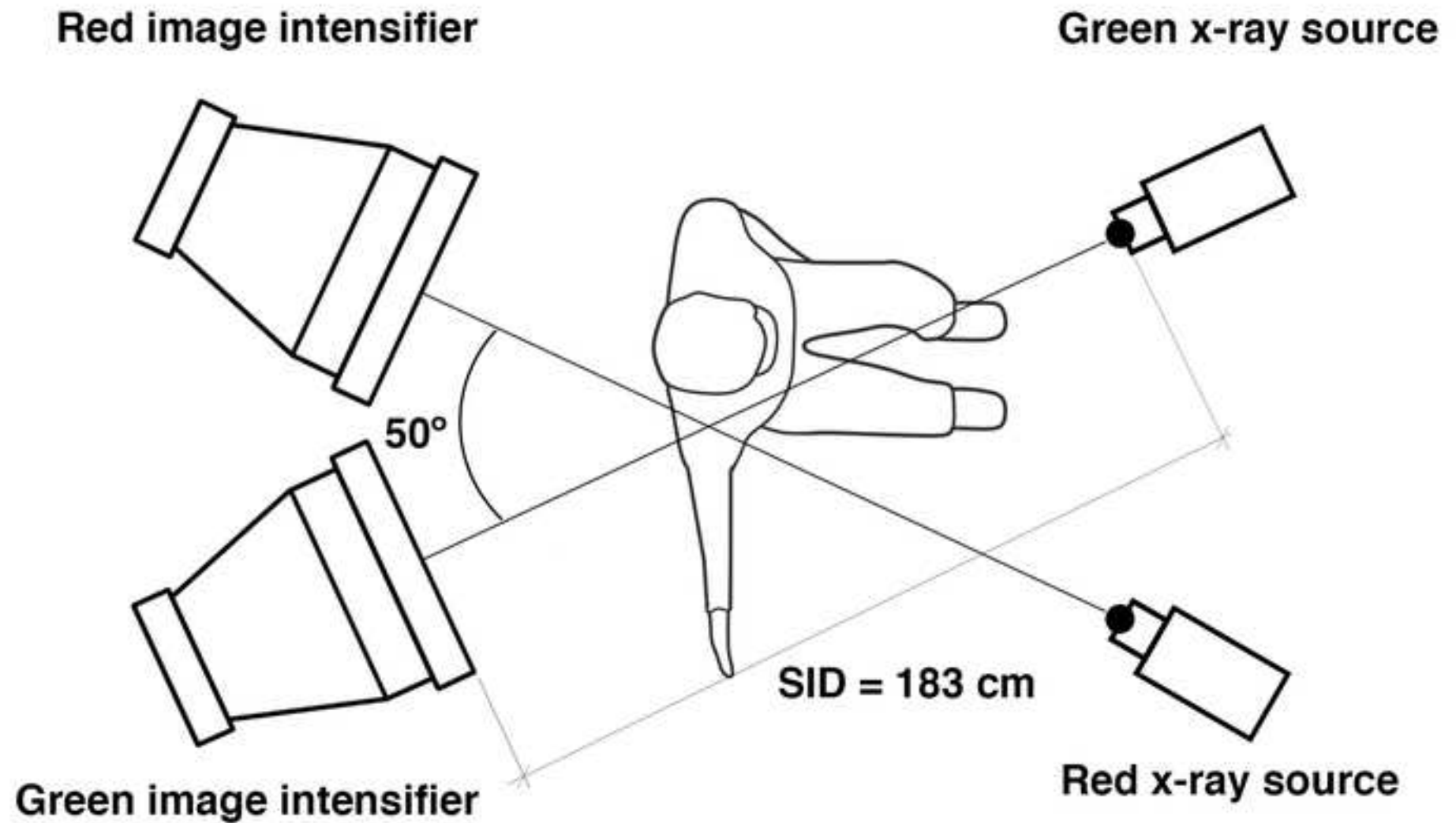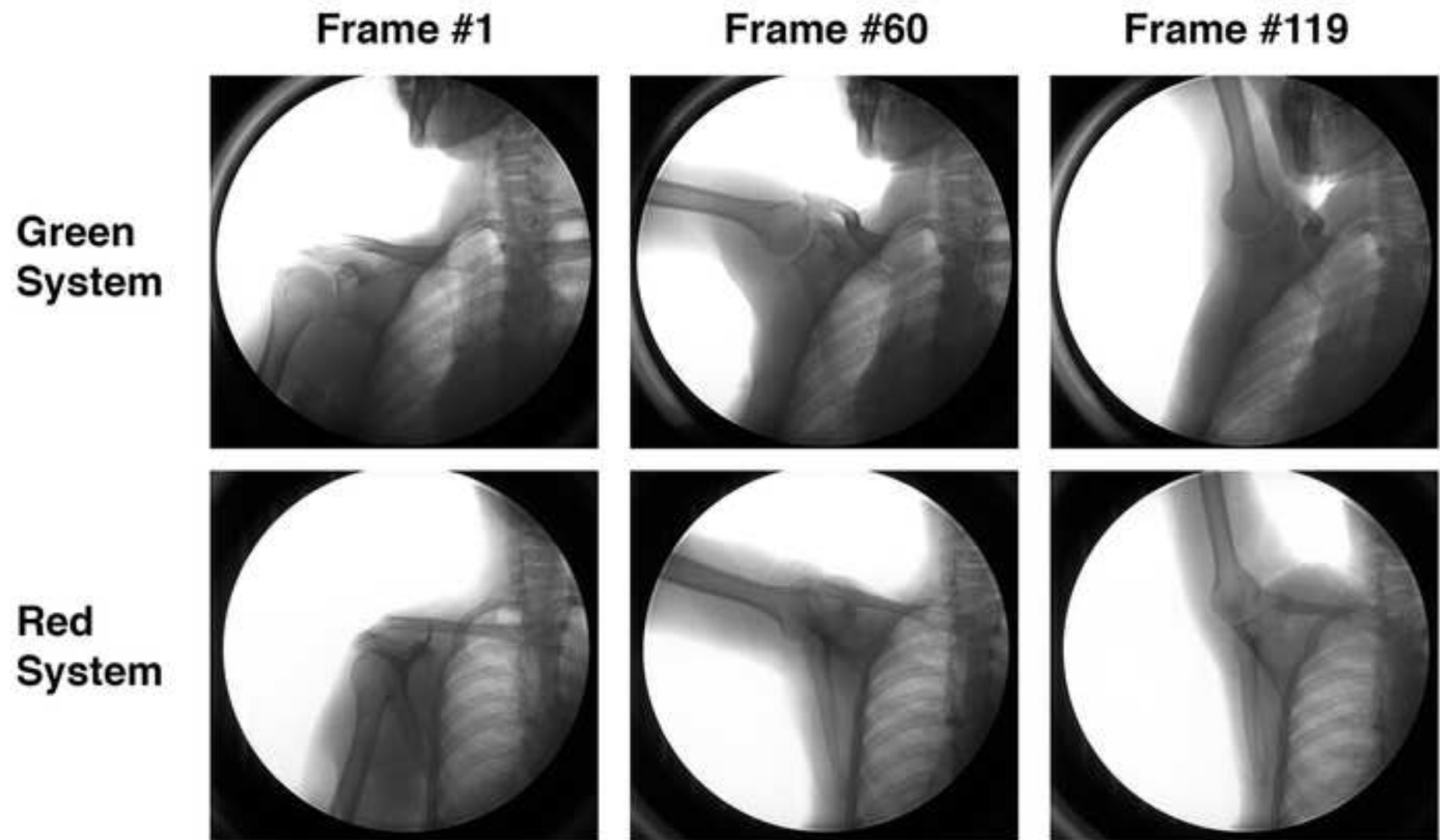
Figure6
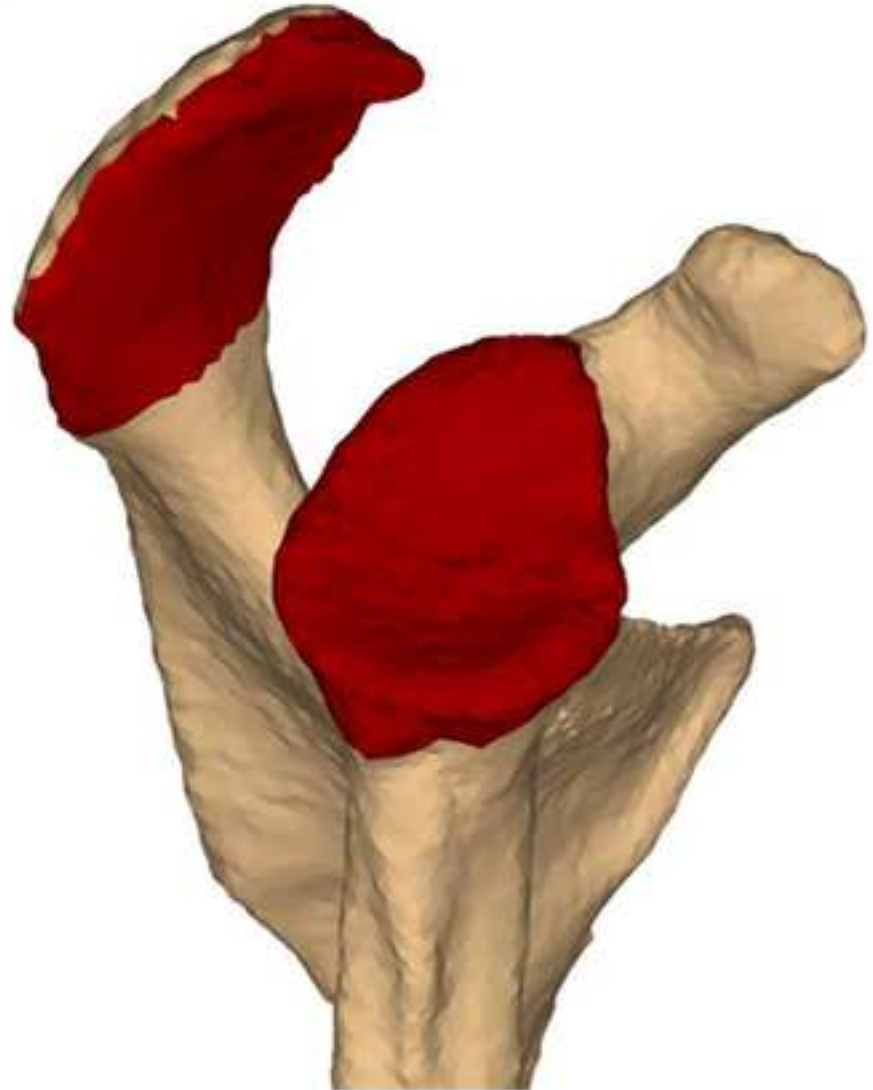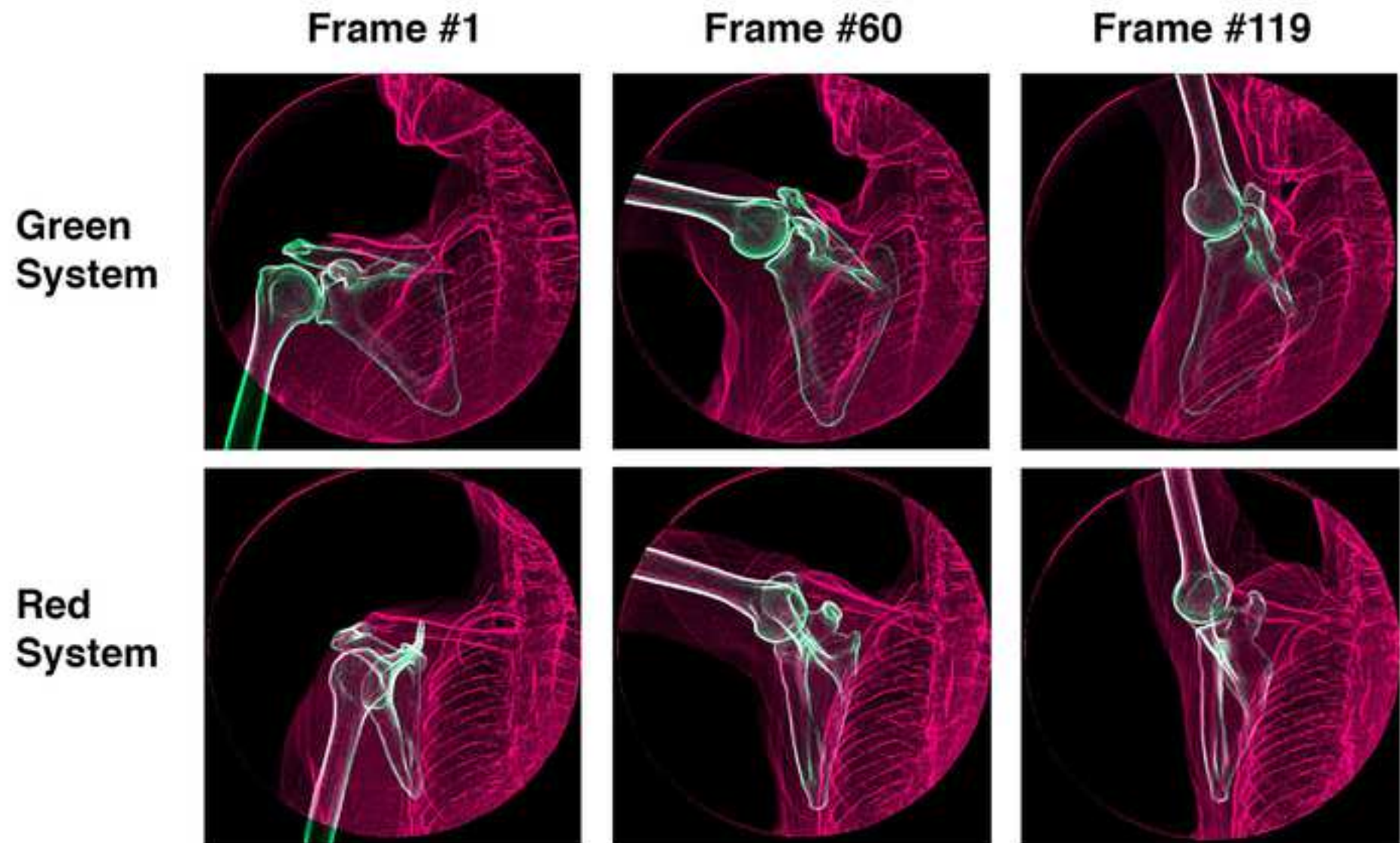
Figure7

Figure8

Figure9

Click here to access/download;Figure;Figure 9.jpg ⬇

Figure10

Figure11

Figure12
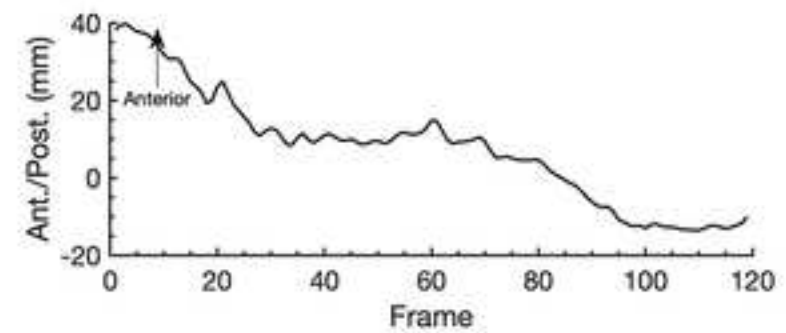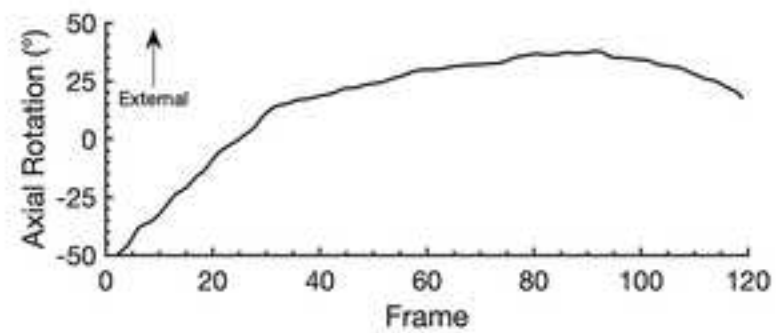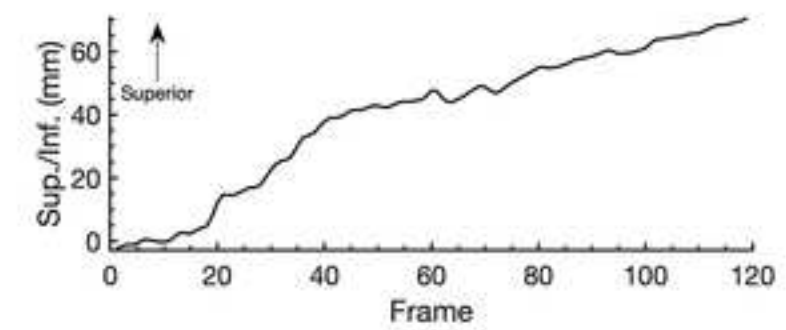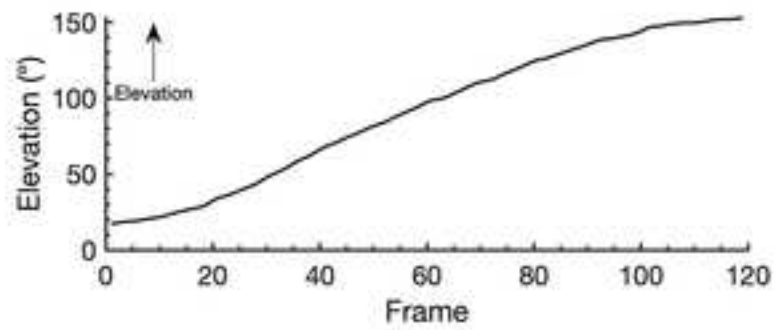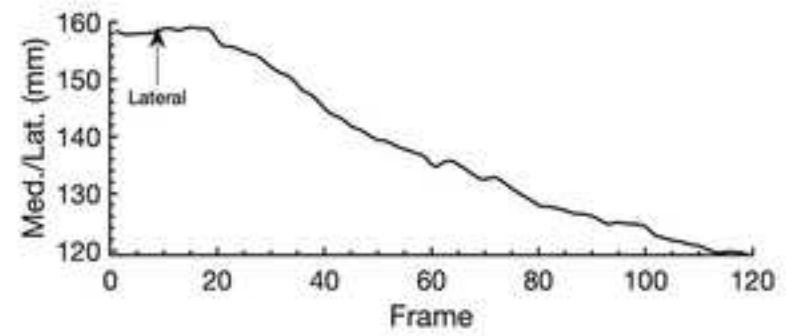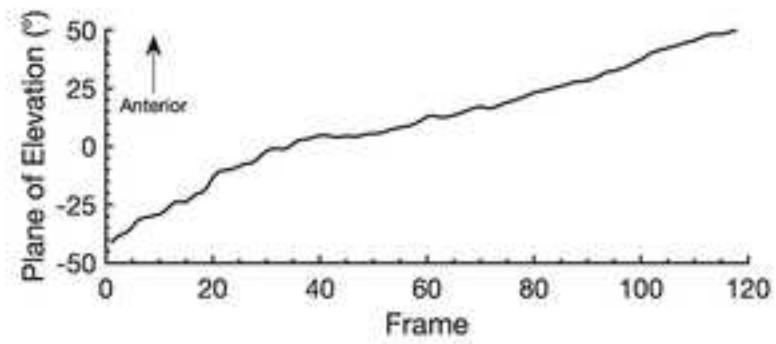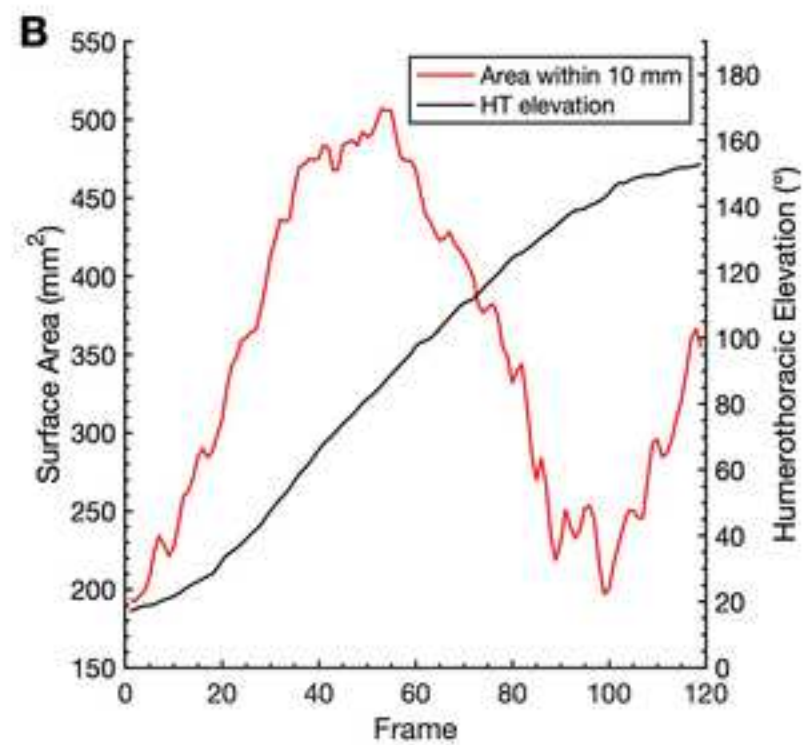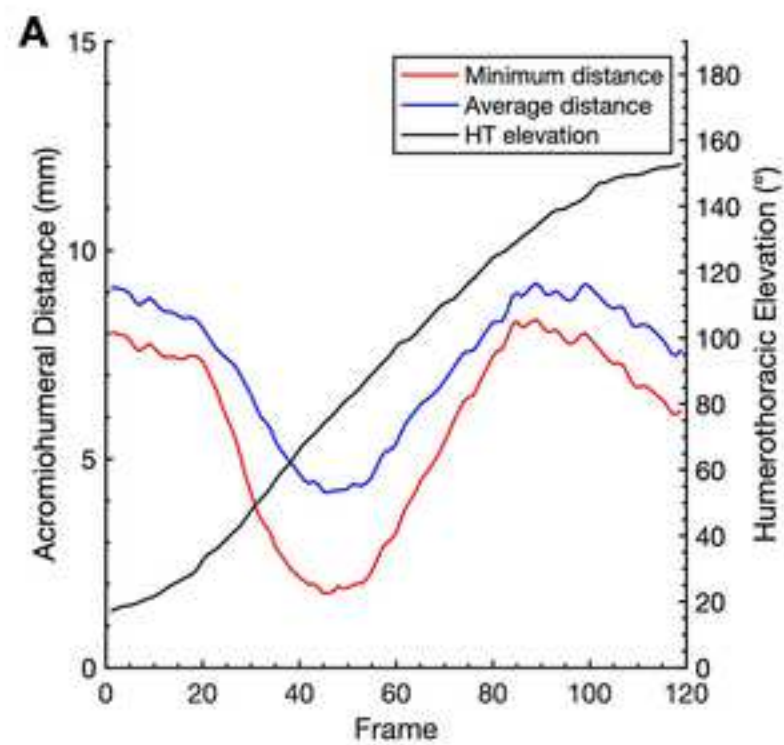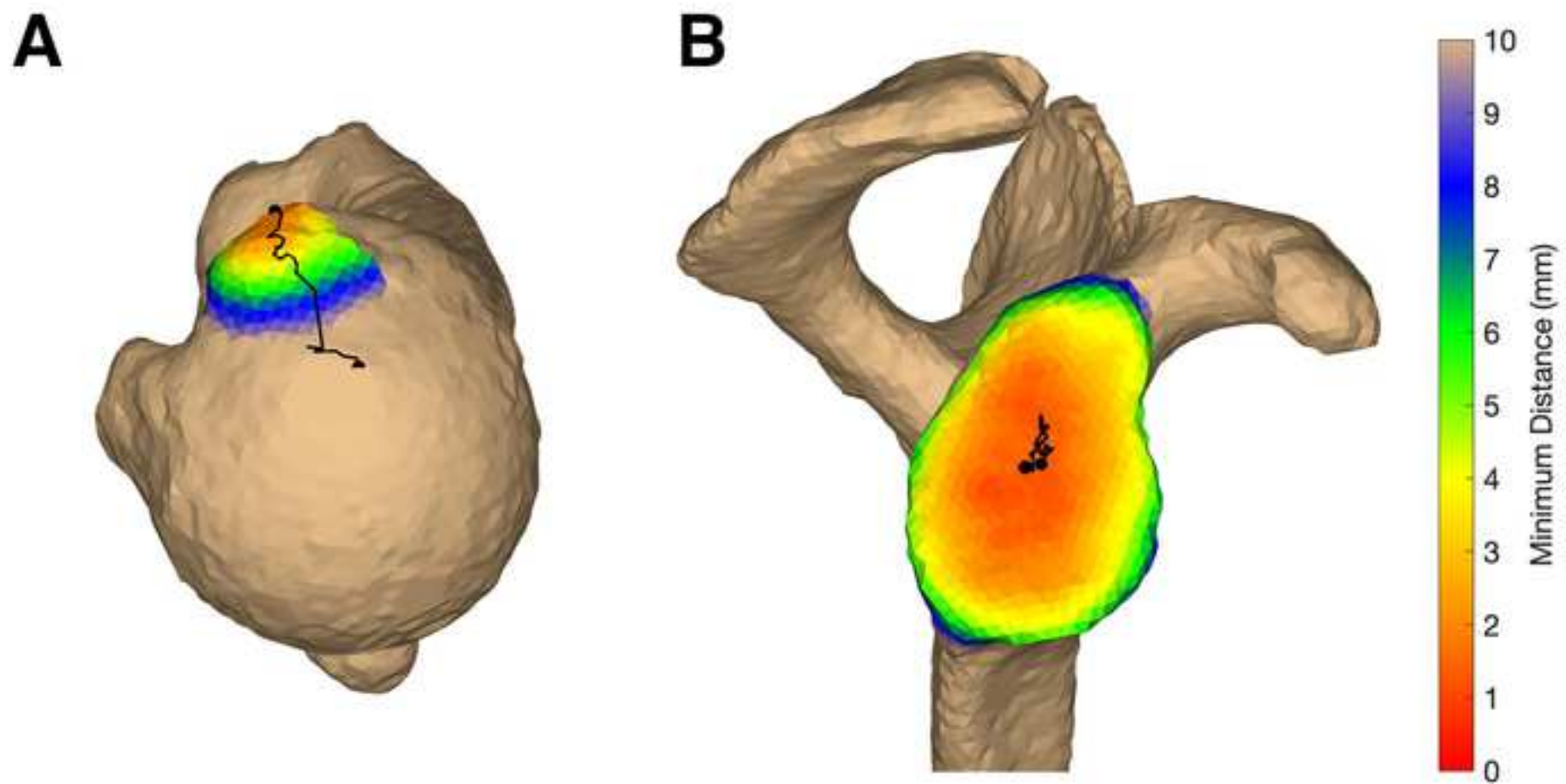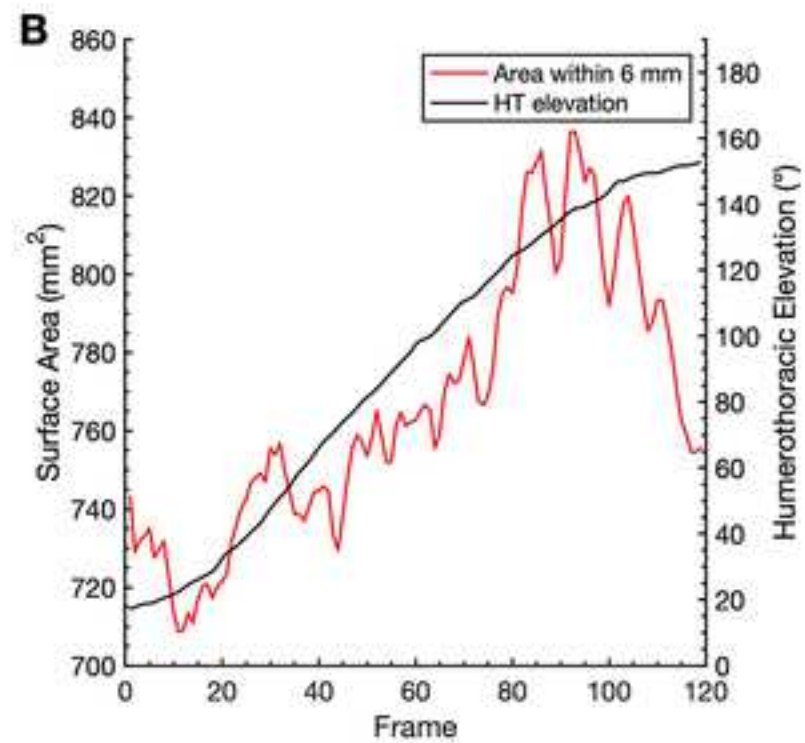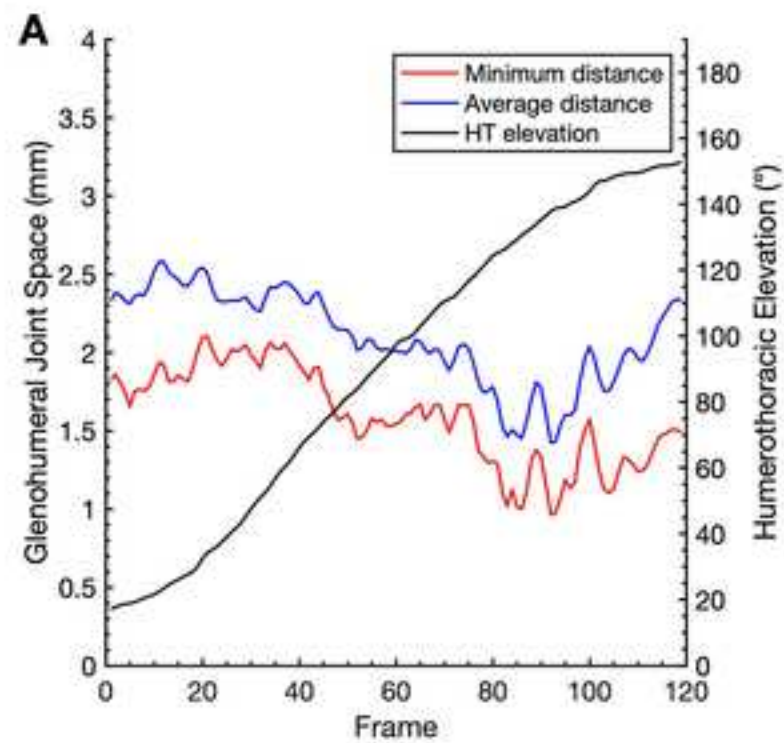
Name of Material/ Equipment	Company	Catalog Number
Calibration cube	Built in-house	N/A
Distortion correction grid	Built in-house	N/A
ImageJ	National Institutes of Health	N/A
Markerless Tracking Workbench	Custom, in house software	N/A
MATLAB	Mathworks, Inc	N/A
Mimics (version 20)	Materialise, Inc	N/A
Open Inventor	Thermo Fisher Scientific	N/A
Phantom Camera Control (PCC) software (version 3.4)		N/A
Pulse generator (Model 9514)	Quantum Composers, Inc.	N/A
Two 100 kW pulsed x-ray generators (Model CPX 3100CV)	EMD Technologies	N/A
Two 40 cm image intensifiers (Model P9447H110)	North American Imaging	N/A
Two Phantom VEO 340 cameras	Vision Research	N/A

Comments/Description

10 cm Lucite box with a tantalum bead in each corner and four additional beads midway along the box's vertical edges (12 beads total). The positions of each bead are precisely known relative to a corner of the box that serves as the origin of the laboratory coordinate system.

Lucite sheet that covers the entire face of the 16 inch image intensifier and contains an orthogonal array of tantalum beads spaced at 1 cm.

Image processing software used to prepare TIFF stack of bone volumes.

A workbench of custom software used to digitize anatomical landmarks on 3D bone models, constructs anatomical coordinate systems, uses intensity-based image registration to perform markerless tracking, and calculates and visualize kinematic outcomes measures.

Computer programming software. For used to perform data processing and analysis.

Image processing software used to segment humerus, scapula, and ribs from CT scan.

3D graphics program used to visualize bones

Software for specifying camera parameters, and acquiring and saving radiographic images

Syncs the x-ray and camera systems and specifies the exposure time

Generates the x-rays used to produce radiographic images

Converts x-rays into photons to produce visible image

High speed cameras record the visible image created by the x-ray system

The claims of the submission do not fit the provided data. Please provide more data or revise the claims in the submission.

Thank you for your thorough review. We have carefully considered the reviewers' comments and have provided additional data to support the claims of the submission as indicated in the responses below.

Please note that the reviewers raised some significant concerns regarding your method and your manuscript. Please revise the manuscript to thoroughly address these concerns. Additionally, please describe the changes that have been made or provide explanations if the comment is not addressed in a rebuttal letter. We may send the revised manuscript and the rebuttal letter back to peer review.

Editorial comments:
Changes to be made by the Author(s):
1. Please take this opportunity to thoroughly proofread the manuscript to ensure that there are no spelling or grammar issues.

The manuscript has been carefully reviewed for spelling and grammar.

2. Please ensure that the references appear as the following: [Lastname, F.I., LastName, F.I., LastName, F.I. Article Title. Source. Volume (Issue), FirstPage – LastPage (YEAR).]

References have been edited to match the format above. However, please note that there was some confusion on our part because what is specified above does not match the "JoVE instructions for authors.docx" file that is available on the website, or the Endnote style file that is referenced in the instructions.

3. Please include the journal name in full for all references.

References have been edited to match the format above.

4. Please adjust the numbering of the Protocol to follow the JoVE Instructions for Authors. For example, 1 should be followed by 1.1 and then 1.1.1 and 1.1.2 if necessary. Please refrain from using bullets or dashes. Please include a line space between all protocol sub-steps.

The numbering within the protocol has been revised and lines have been added between protocol sub-steps. Note: to avoid excessive track changes annotation, these changes were made untracked.

5. Please highlight up to 3 pages of the Protocol (including headings and spacing) that identifies the essential steps of the protocol for the video, i.e., the steps that should be visualized to tell the most cohesive story of the Protocol. Remember that non-highlighted Protocol steps will remain in the manuscript, and therefore will still be available to the reader. Currently, only section headers are highlighted.

Highlighting has been added to the essential steps.

6. Please ensure that the highlighted steps form a cohesive narrative with a logical flow from one highlighted step to the next. Please highlight complete sentences (not parts of

sentences). Please ensure that the highlighted part of the step includes at least one action that is written in imperative tense.

This requirement has been verified. Imperative tense is used in several steps (e.g., 2.4.13, 2.6.2).

7. Please include all relevant details that are required to perform the step in the highlighting. For example: If step 2.5 is highlighted for filming and the details of how to perform the step are given in steps 2.5.1 and 2.5.2, then the sub-steps where the details are provided must be highlighted.

This requirement has been verified.

8. Are the custom software used for the points 3-5 in the protocol open source? Can any further details (e.g., code) be provided?

Unfortunately, the custom software is not open source. The manuscript has been modified to acknowledge this (by using the term "proprietary") and to suggest other software that can be used to complete the step of the protocol (step 3.5):
> Markerless tracking is performed using proprietary software. Software such as Autoscoper and C-Motion can also be used to complete this process.

9. Please provide a statement stating that ethics approval was obtained for the human studies.

This statement is made in the first paragraph of the Representative Results: "Prior to data collection, the participant provided written informed consent. The investigation was approved by Henry Ford Health System's Institutional Review Board."

Reviewer #1:
Manuscript Summary:
The manuscript is a well written protocol for measuring shoulder kinematics using biplane fluoroscopy. The steps could be easily followed, and there is appropriate commentary on where protocol deviations may exist.

Thank you for this feedback.

Major Concerns:
The accuracy or efficacy of the method is not discussed. The authors give one example of using the protocol to measure shoulder kinematics, but with no comparison method, they cannot comment on the accuracy. Without the ability to highlight accuracy, the benefit of this method over non-ionizing methods is unclear.

Thank you for this comment. The accuracy of the system was referenced but not explicitly stated in the discussion. We have revised the discussion to explicitly state the accuracy of the system and the manner in which it was tested:
> "The accuracy of the protocol described herein was established for the glenohumeral joint against the gold standard of radiostereometric analysis (RSA) to be ±0.5° and ±0.4 mm."

Reviewer #2:

Review for Manuscript number JoVE62210 titled "Measuring 3D in-vivo shoulder kinematics using biplanar videoradiography"

General comments
This manuscript describes detailed methods used by the authors to measure joint motion at the shoulder using biplane videoradiography. While the main emphasis is on the methods, kinematic results for measurements taken for one activity for a single study participant are also presented. In my opinion, the paper is written clearly and may help other researchers who intend to use biplane x-ray imaging for measuring shoulder joint motion.

Major Concerns
My main concern in relation to this manuscript is that although the main focus of the manuscript is on the methods of measurement, and the importance of measuring joint kinematics accurately have been emphasized throughout the paper, no effort has been made to quantify the measurement accuracy associated with these methods in assessing shoulder joint kinematics. I think this is a serious limitation of the manuscript which needs addressing. I also believe that addressing this limitation would greatly increase the value of this paper and encourage other researchers to adopt the methods described here.

Thank you for this comment. The accuracy of the system was referenced but not explicitly stated in the discussion. We have revised the discussion to explicitly state the accuracy of the system and the manner in which it was tested.
> "The accuracy of the protocol described herein was established for the glenohumeral joint against the gold standard of radiostereometric analysis (RSA) to be ±0.5° and ±0.4 mm."

Detailed Comments
Introduction
Since this paper is focused on the method (or a series of methods) to capture biplane X-ray images and use them to measure kinematics at a human joint it would be a good idea to introduce the reader to the methods that are already presented in the literature. I suggest referencing some of the earlier work that was done in this field by the likes of Scott Tashman as they have established several of the steps for the knee joint which are used in your work. I fully appreciate that the current paper is based on the shoulder and that there are several steps in the methods that are unique to the shoulder.

Thank you for this feedback. It is our understanding that other researchers will submit similar manuscripts but for other joints (e.g., knee) for this special issue. As such, we intentionally focused this manuscript on the methods and special consideration for measuring shoulder kinematics. However, we have added a statement in the discussion that these methods can be modified for measuring human motion at other joints and have provided appropriate references for other researchers (e.g., Tashman) who have done so.
> The accuracy of the protocol described herein was established for the glenohumeral joint against the gold standard of radiostereometric analysis (RSA) to be ±0.5° and ±0.4 mm. Similar protocols have been developed for other joints such as the knee, spine, and foot/ankle.

Lines 55-58: Please give references here to support these claims.

Appropriate references have been made to support the statements.

Protocol
Lines 103-105 Consider giving a diagram perhaps with three views to show the region described.

Thank you for this suggestion. A figure (Figure 1) has been added showing the region described in three views.

Line 277: Change 'while field' to 'white-field' if that is what was meant here.

Thank you for identifying this typographical error. The edit has been made.

Line 287: Mistake in this sentence needs correcting.

Thank you for identifying this error. The edit has been made.

Lines 358-365: Is it right to assume that a large number of piecewise linear transformations from the distorted image to the undistorted image were created? Why was this technique used for distortion correction instead of the widely used polynomial model-based methods used by others (e.g. 9th order polynomial models were used by Eric H. Garling 2005)? If a new method is used here, I think more detail needs to be given and its use justified. Discuss (in the Discussion section) how does this method compare with methods used by others especially in terms of accuracy? If other papers have used this method for distortion correction, please refer to them but still justify why this method was used.

Thank you for this question. We agree that there are many algorithms for calculating distortion correction with varying levels of complexity and accuracy. Although our method may use a less complex algorithm, validation studies have suggested that our measurement technique (including the described distortion correction) has been shown to have an accuracy of better than +/- 0.5 mm and +/- 0.5 degrees (Bey et al., J Biom Eng, 2006; Tashman and Anderst J Biomed Eng 2003). It is unclear whether a more advanced distortion correction algorithm would have a substantial impact on accuracy. Even so, the level of accuracy afforded by our protocol is sufficient for the purposes of tracking in-vivo shoulder kinematics.

Lines 407-408: This step is not clear needs to be more specific. What are conventional methods in this context? Please give some detail or at least the name of the method used.
Thank you for this clarifying question. We have revised the manuscript to more clearly describe this step, and also provided references for how to define these coordinate systems. Step 4.1.1 now reads:

> For each bone and frame of motion, use the filtered anatomical landmark coordinates (i.e., output from the markerless tracking software) to construct a 16-element transformation matrix representing the bone's anatomical coordinate system relative to the laboratory coordinate system.

Lines 416-417: The value one gets from this method may vary significantly based on triangle size. Triangle centers on opposing bones will not align with each other so that the minimum distance between surfaces is equal to the minimum distance between centers of triangles. Was a convergence test done with triangle edge size? If not how was triangle size selected? What was the edge length used?

Thank you for this question. The resolution of the triangular mesh (and thus the length of the triangle edges) was scaled to the voxel spacing. We felt this was the most logical resolution given the most geometrically "correct" triangle size should be based on the natural sampling of the CT volume. To acknowledge the details of the model rendering, step 3.2.1 now reads.

> Import the TIFF image stack for the bone to be processed. The proprietary software converts the TIFF stack to a .RAW file and renders a 3D bone model based on the known pixel dimensions and image spacing. Import the TIFF image stack for the bone to be processed. The custom software converts the TIFF stack to a .RAW file and renders a 3D bone model based on the known pixel dimensions and image spacing. The resolution of the model is based on the sampling of the CT volume (i.e., voxel spacing). Consequently, the average area of the mesh triangles is approximately 1.02 mm^2 (±0.2 mm^2) given the CT protocol describe in this protocol (step 1.3).

Line 421: Why was 200mm^2 used? Justify this selection. Will larger bones need a larger area to be used?

Thank you for this question. This measurement area was included in the calculation to ensure that only the surface that was reasonably near to the opposite bone is included in the average gap calculation. The magnitude of the measurement area (i.e., 200 mm2) was selected during initial algorithm development after it was found to consistently reflect proximities without being overly biased from distant surfaces. Also, the size of the bone is not necessarily the important factor in the determination of the size of the measurement area. Instead, the amount of interaction between the surfaces (i.e., how much area is near/far between surfaces) is the more important determinant. This is because selecting a measurement area too small will ignore potentially important surface interactions, while selecting a measurement area too large will include distant (and therefore irrelevant) interactions. We have also clarified the choice of this measurement area for glenohumeral and subacromial proximities, and that other broader surface interactions (e.g., tibiofemoral) may require a larger measurement area. The manuscript has been revised to include these considerations (step 4.1.5):

> This measurement area was included in the calculation to ensure that only the surface that was reasonably near to the opposite bone is included in the average gap calculation. Note: the size of the measurement area (i.e., 200 mm^2) was selected during initial algorithm development after it was found to consistently reflect subacromial space and glenohumeral joint proximities without being overly biased from distant surfaces. Use of this measure for broader surface interactions (e.g., tibiofemoral) may require a larger measurement area.

Lines 422-427: This point (1.6) is not clear. Please consider making it clearer.

Thank you for this question. We have revised the statement, which now reads (lines step 4.1.6):

> Weighted-average contact center (i.e., centroid): Calculated as the point on the ROI surface that minimizes the weighted distance to all other triangles within the measurement area (i.e., triangles closest to the opposite bone whose areas sum to 200 mm^2). The weighting factor for each triangle in the measurement area is calculated as: triangle area / squared distance to nearest-neighbor centroid (i.e., inverse square weighting). In this way, the triangles that are weighted more heavily are larger (by a factor of 1) and closer to the opposite bone (by a factor of the squared minimum distance).

Lines 428-429: This text suggests that a single point is calculated across the activity. Is that what was done? If so, what is the significance of that point?

Thank you for this question. The average contact center represents the average position of the contact center across the motion trial. In other words, the average location of the centroid between the surfaces across the motion. Given contact centers represent joint arthrokinematics, the average contact center would indicate the center of surface interactions during a movement. This is clarified in the manuscript (lines 4.1.7):

> "Average contact center: Calculated as the average position of the contact center (i.e., centroid) across the motion trial. Given contact centers represent joint arthrokinematics, the average contact center represents the center of surface interactions during a movement."

Line 483: The caption says 60° while the associated figure says 50°. What was the actual value you used?

Thank you for catching this typographical error in the figure legend. The legend has been revised accordingly.

Discussion
Since this is a methods-based paper, I think it would be good to discuss what is different in the methods presented here that are different from those published by other authors. Discuss how they are different and their relative advantages and disadvantages. For example, the method used for distortion correction appears to be inferior (I could be wrong) to what others have used (e.g. 9th order polynomial model was used by Eric H. Garling 2005). Whether inferior or superior I think your methods need to be discussed alongside those of others'.

Thank you for this question. As we described above, we agree that there are many algorithms for calculating distortion correction with varying levels of complexity and accuracy. However, we believe that comparing these various methods is outside the scope of this paper and including such a discussion would require the removal of practical considerations that fulfill the stated purpose of the manuscript.

Lines 574-574: Please explain how increasing the distance between the source and the subject would reduce the radiation exposure to the subject in this specific instance. Assuming that image brightness at the region of interest remains unchanged, how would the distance between the source and the subject change exposure. Readers may find this interesting. (I understand how the inverse square law will apply to reduce the exposure for a bystander not being imaged, but don't see how this applies to the person being imaged.)

Thank you for this insight. We agree with your assessment and have revised the manuscript by removing this consideration.

Several lines in the Discussion section emphasize the importance of measuring kinematics accurately. E.g. Lines 542-549, 551-552, 629-631. I completely agree with the authors that accuracy is important. However, the authors give no indication of the accuracy of their methods and system in measuring kinematics at the shoulder. I think this is the most significant weakness of the paper and needs to be addressed.

Thank you for this comment. The accuracy of the system was referenced but not explicitly stated in the discussion. We have revised the discussion to explicitly state the accuracy of the system and the manner in which it was tested:

"The accuracy of the protocol described herein was established for the glenohumeral joint against the gold standard of radiostereometric analysis (RSA) to be ±0.5° and ±0.4 mm."